Article

Stereochemistry in the disorder–order continuum of protein interactions

https://doi.org/10.1038/s41586-024-08271-6

Received: 25 January 2024

Accepted: 22 October 2024

Published online: 27 November 2024

Open access

Check for updates

Estella A. Newcombe[1,2,3,6], Amanda D. Due[1,2,3,6], Andrea Sottini[4], Steffie Elkjær[1,3], Frederik Friis Theisen[1,2,3], Catarina B. Fernandes[1,2,3], Lasse Staby[1,2,3], Elise Delaforge[1,2,3], Christian R. O. Bartling[5], Inna Brakti[1,2,3], Katrine Bugge[1,2,3], Benjamin Schuler[4], Karen Skriver[1,3], Johan G. Olsen[1,2,3] ✉ & Birthe B. Kragelund[1,2,3] ✉

Intrinsically disordered proteins can bind via the formation of highly disordered protein complexes without the formation of three-dimensional structure[1]. Most naturally occurring proteins are levorotatory (L)—that is, made up only of L-amino acids—imprinting molecular structure and communication with stereochemistry[2]. By contrast, their mirror-image dextrorotatory (D)-amino acids are rare in nature. Whether disordered protein complexes are truly independent of chiral constraints is not clear. Here, to investigate the chiral constraints of disordered protein–protein interactions, we chose as representative examples a set of five interacting protein pairs covering the disorder–order continuum. By observing the natural ligands and their stereochemical mirror images in free and bound states, we found that chirality was inconsequential in a fully disordered complex. However, if the interaction relied on the ligand undergoing extensive coupled folding and binding, correct stereochemistry was essential. Between these extremes, binding could be observed for the D-ligand with a strength that correlated with disorder in the final complex. These findings have important implications for our understanding of the molecular processes that lead to complex formation, the use of D-peptides in drug discovery and the chemistry of protein evolution of the first living entities on Earth.

The stereochemistry of amino acids, and therefore of proteins, is biological canon. The chirality of the C^{α} atom means that the mirror images (enantiomers) of amino acids cannot be superimposed—that is, they have a 'handedness'. Amino acids in nature are predominantly 'left-handed' or levorotatory (L), whereas their enantiomers are 'right-handed' or dextrorotatory (D) (Fig. 1a)—so named because of how they affect circularly polarized light[3]. Thus, L- and D-amino acids and proteins composed of L- and D-amino acids (L- and D-proteins, respectively) are mirror images of each other (Fig. 1b). The preference for L-proteins is so strong that we may generally say that L-proteins make up the molecular structure and machinery of Nature. However, D-amino acids do exist, and Nature typically exploits these in signalling, as free amino acids, or in defence systems, as parts of short peptides, or in peptidoglycans (for example, in the bacterial cell wall[4,5]), as neurotransmitters[6], toxins and venoms[7], and as antibiotics[8] (reviewed in ref. 9).

Proteins are key to the activity of biological systems; they function through interactions with one or several binding partners. It is widely accepted that the D-enantiomer of a protein would be unable to bind a partner L-protein. However, in a pharmaceutical context, it would be desirable to overcome this lack of binding, owing to the metabolic stability of D-peptides in biological systems, where they are not recognized by natural metabolic processes[10]. Thus, peptides based on D-amino acids have been explored as constituents of peptide drugs and synthetic D-proteins have been used as scaffolds for screening natural or de novo designed L-peptides in mirror-image phage displays[11,12]. In the 'retro-inverso' strategy, D-amino acid-based peptides mimic the L-peptide enantiomer when the D-amino acid sequence is produced in reverse[13]. This strategy relies on the D-peptide forming the same secondary structure as the L-peptide, enabling interaction with its L-protein binding partners. Examples can be found in the treatment of diabetes[14,15], breast cancer[16] and inflammation[17].

The past 25 years have uncovered the functional relevance of intrinsically disordered proteins and protein regions (referred to collectively here as IDPs) existing in dynamic ensembles of interconverting conformations[1]. Although structural disorder can persist in complexes and has important functional roles there, it remains unclear whether IDPs are confined to chiral constraints[18–20]. The continuum of complexes formed by IDPs ranges from folded, induced-fit interactions to fuzzy, or fully disordered complexes with structural heterogeneity[21,22]. Not much is known about the atomic structure of heterogeneous complexes, and less is known about the structure of fully disordered complexes where the ligand at the extreme can be comparably dynamic in the free and the bound states[22,23]. This raises the fundamental question of whether these complexes are truly independent of 3D topology and

[1]REPIN, Department of Biology, University of Copenhagen, Copenhagen N, Denmark. [2]Structural Biology and NMR Laboratory, Department of Biology, University of Copenhagen, Copenhagen N, Denmark. [3]Linderstrøm Lang Centre for Protein Science, Department of Biology, University of Copenhagen, Copenhagen N, Denmark. [4]Department of Biochemistry and Department of Physics, University of Zurich, Zurich, Switzerland. [5]Department of Drug Design and Pharmacology, Center for Biopharmaceuticals, University of Copenhagen, Copenhagen, Denmark. [6]These authors contributed equally: Estella A. Newcombe, Amanda D. Due. ✉e-mail: joe@bio.ku.dk; bbk@bio.ku.dk

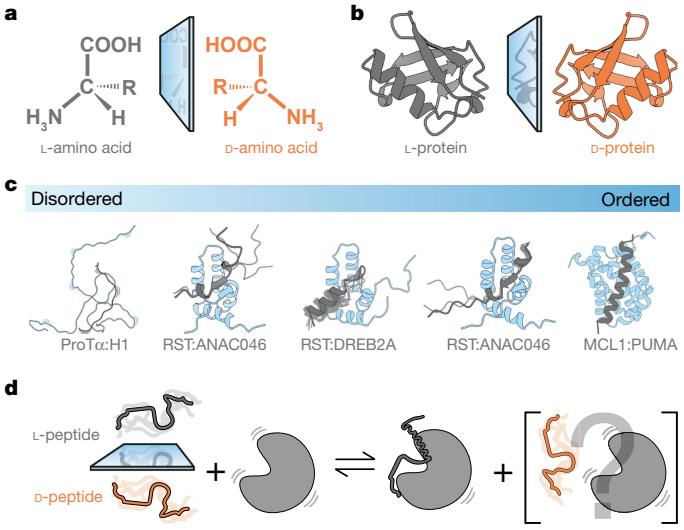

Fig. 1 | Chirality in protein–protein interactions. a,**b**, L- and D-amino acids (**a**) and L- and D-proteins are mirror images of each other, illustrated in **b** by ubiquitin (Protein Data Bank (PDB): 4GSW). **c**, The five protein pairs constituting our model system covering a continuum of disordered (ProTα:H1)[22,24] to ordered (MCL1:PUMA)[25] protein complexes, and three intermediate interactions of RST with ANAC046, DREB2A[28] and ANAC013. **d**, L-protein pairs will interact, but the features that might allow L-proteins and D-proteins to interact are unclear.

thus independent of the chiral constraints of folded complexes, or whether there are configurational constraints, perhaps too subtle to be resolved experimentally.

To answer this question, we selected an assortment of interacting protein pairs in which the ligand is disordered in its unbound state, and either stays disordered in the complex or adopts different degrees of structure upon binding (Fig. 1c). Peptide ligands were synthesized using D-amino acids and their binding to folded partners was compared to that of their L-peptide enantiomers using a range of biophysical and structural methodologies (Fig. 1d). We found that sensitivity to chirality in binding correlates with retained disorder in the complex, with fully disordered protein complexes forming regardless of the 'handedness' of the ligand.

To test whether disordered protein interactions could persist regardless of chirality, we initially focused on the interaction of prothymosin-α (ProTα) with histone H1.0 (H1), which has been shown to be a high-affinity, disordered interaction[22,24] (Fig. 1c). We used a 21-residue peptide from the C-terminal tail of H1, $H1_{155–175}$ (Fig. 2a), which contains a high charge density with a fraction of charged residues of 0.52 (Extended Data Table 1), and procured L- and D-enantiomers (L-$H1_{155–175}$ and D-$H1_{155–175}$). Far-UV circular dichroism (CD) confirmed that the two peptides were mirror images of each other (Fig. 2b), and nuclear magnetic resonance (NMR) spectroscopy analyses showed identical chemical shifts (Extended Data Fig. 1a). The CD spectra also showed that the peptides were disordered, as expected. We next used NMR to measure the chemical shift perturbations (CSPs) of ProTα caused by each enantiomer upon their addition. In this case, we found that L-$H1_{155–175}$ and D-$H1_{155–175}$ produced similar CSPs in ProTα (Fig. 2c), which we quantified by calculating the difference between the CSPs induced by L- and D-enantiomers ($\Delta CSP_{L\text{-}D}$) at equimolar concentrations of each enantiomer of the $H1_{155–175}$ peptide (Fig. 2d). We probed the affinity (K_d) and thermodynamic properties using isothermal titration calorimetry (ITC), finding the same values for the enantiomers in terms of K_d (Fig. 2e and Extended Data Table 2). We observed that the changes in binding enthalpy ($-T\Delta S$) and entropy (ΔH) were similar for L-$H1_{155–175}$ and D-$H1_{155–175}$ (Extended Data Table 2), and that the K_d value was in the low micromolar range for both enantiomers. ProTα and full-length H1 interact with nanomolar to picomolar affinity at near-physiological ionic strength[22,24], but we observed micromolar affinity with the peptides, mostly because of the lower total charge of the $H1_{155–175}$ fragment (ProTα: −43 (or −44 depending on isoform[24]); L/D-$H1_{155–175}$: + 11; full-length H1: + 53). We also obtained binding affinities using single-molecule Förster resonance energy transfer (smFRET) spectroscopy, labelling ProTα with donor and acceptor fluorophores (Fig. 2f). The agreement between the affinities obtained by ITC and smFRET using very different ProTα concentrations suggests that the complex is predominantly of 1:1 stoichiometry (Fig. 2). Furthermore, analogous to the NMR CSPs, the smFRET data showed that the changes in transfer efficiencies on binding are very similar for L-$H1_{155–175}$ and D-$H1_{155–175}$, indicating that the conformational ensembles of ProTα bound to L-$H1_{155–175}$ or D-$H1_{155–175}$ are highly similar, again highlighting that there is no significant difference between the interactions of ProTα with the L- or D-enantiomers of $H1_{155–175}$.

As an example, representing the other end of the disorder–order continuum, we probed the interaction between induced myeloid leukaemia cell differentiation protein (MCL1) and p53 upregulated modulator of apoptosis (PUMA, also known as Bcl-2-binding component 3) L- and D-peptides (Extended Data Table 1). This nanomolar-affinity complex has previously been characterized as a folding-upon-binding induced-fit interaction that leads to the folding of disordered $PUMA_{130–156}$ into a stable α-helix within the complex[25] (Figs. 1c and 2g). We therefore postulated that the D-enantiomer of PUMA would be unlikely to bind MCL1. As PUMA tends to form homodimers in solution, we used the strictly monomeric M144I variant, which is a fully functional binding partner of MCL1[26]. Far-UV CD and NMR analyses indicated that the PUMA peptide was disordered, with L- and D- enantiomers producing mirror-image CD spectra and identical chemical shifts (Fig. 2h and Extended Data Fig. 1). We first performed ITC using the same concentrations for both L-PUMA and D-PUMA, finding that L-PUMA bound with nanomolar affinity, whereas D-PUMA appeared not to bind (Fig. 2i and Extended Data Table 2). By increasing the concentrations of both MCL1 and D-PUMA considerably, we were able to observe a K_d value in the high micromolar to low millimolar range (Fig. 2j). All thermodynamic properties (Extended Data Table 2) were very different for L-PUMA and D-PUMA, which further suggests that there is a fundamental difference between L-PUMA and D-PUMA in their ability to interact with MCL1. We then compared the NMR CSPs induced at equally saturated levels (90% bound) of either L-PUMA or D-PUMA to MCL1. Only L-PUMA caused substantial CSPs for MCL1 (Fig. 2k). Since the interaction between MCL1 and L-PUMA was in slow exchange on the NMR timescale, the relative contributions of the bound and unbound species could be assessed from relative peak intensities. Reduced intensity of peaks representing the free state of MCL1 was observed in the presence of D-PUMA, suggesting some compatibility but a failure to achieve the folded bound state, as also supported by the very small chemical shift changes in MCL1 (Fig. 2l). This might indicate that D-PUMA can interact weakly with MCL1 but cannot undergo the folding required for an induced-fit interaction.

Overall, using L- and D-peptides and comparing interactions at the extremes of the disorder–order continuum confirms the need for homochirality in structurally ordered complexes. However, a fully disordered heterochiral complex can form, even with binding characteristics that are indistinguishable from the natural counterpart.

Having probed the extremes of the disorder–order continuum, the next step was to understand how intermediate systems respond to chirality. As intermediate systems, we used the RCD1–SRO–TAF4 (RST) domain from RCD1, interacting with various transcription factors that form different degrees of structure in their RST-bound states[27] (Fig. 1c). We characterized interactions of RST with L- and D-peptides derived from the transcription factors ANAC046 ($ANAC046_{319–338}$; Fig. 3a), DREB2A ($DREB2A_{255–272}$; Fig. 3b) and ANAC013 ($ANAC013_{254–274}$; Fig. 3c

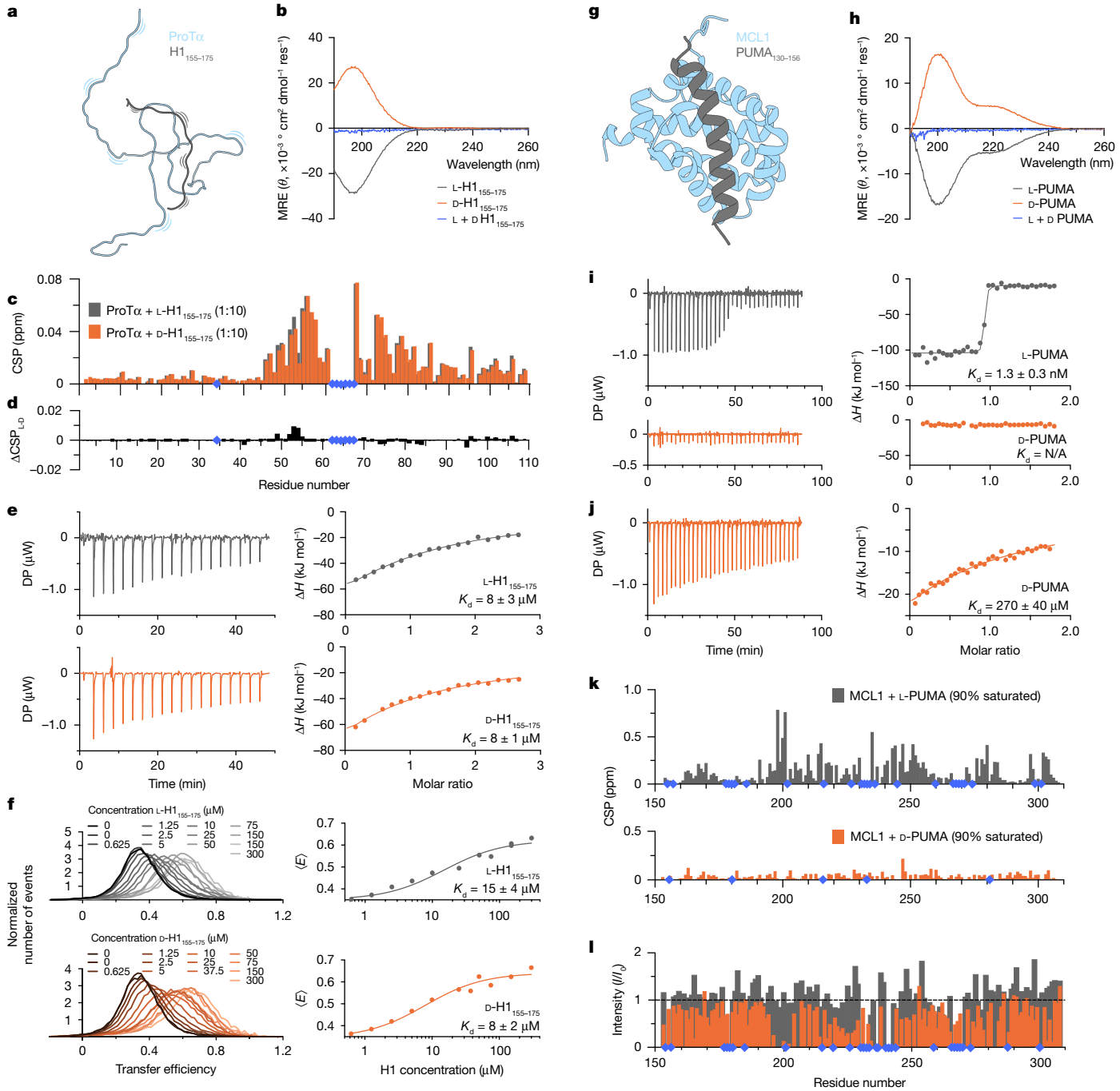

Fig. 2 | Effects of chirality on protein interactions. a, ProTα and the $H1_{155–175}$ peptide remain disordered during their interaction. **b**, Far-UV CD spectra of L-$H1_{155–175}$ and D-$H1_{155–175}$ peptides and their sum. MRE, mean residue ellipticity ($cm^2\ dmol^{-1}$ residue^{-1}; $n = 1$). **c**,**d**, CSP (**c**) and $\Delta CSP_{l\text{-}d}$ ($n = 1$) (**d**) caused by the addition of L-H1 or D-H1 (500 μM) to ProTα (50 μM). **e**, ITC of interactions of ProTα with L-$H1_{155–175}$ and D-$H1_{155–175}$. Raw ITC thermograms (left) and fitted one-site binding isotherms (right). DP, differential power. **f**, smFRET of L-$H1_{155–175}$ or D-$H1_{155–175}$ with ProTα, fitting FRET efficiency ($\langle E \rangle$) as a function of ligand concentration to obtain K_d values. **g**, MCL1 is folded and interacts with the disordered PUMA peptide, which forms an α-helix upon interaction via induced fit. **h**, Far-UV CD spectra of L-PUMA and D-PUMA peptides, and their sum. **i**, ITC performed under the same conditions for both L-PUMA and D-PUMA ($n = 3$, figure is representative). N/A, not applicable. **j**, ITC performed using higher concentrations of both MCL1 and D-PUMA (70 μM and 700 μM, respectively; $n = 3$, figure is representative). **k**, CSPs induced by the interaction of MCL1 (50 μM) with L-PUMA and D-PUMA at equal (90%) saturation ($n = 1$). **l**, Changes in NMR peak intensities upon addition of L-PUMA or D-PUMA to MCL1 at 90% saturation ($n = 1$). In all panels, L-peptides are represented in grey, and D-peptides are in orange. Blue diamonds indicate missing assignments, assigned residues that could not be tracked, or prolines.

and Extended Data Table 1). Previous far-UV CD analyses suggested an induced helical structure for the DREB2A in complex with RST; an effect that was less pronounced for the two other ligands[27]. Whereas an NMR-based HADDOCK model exists for the RST–DREB2A complex[28] (Fig. 3b), the structures formed by ANAC046 and ANAC013 in their complexes with RST were unknown. Thus, we generated a structural prediction for these interactions using AlphaFold3[29,30] (Fig. 3a,c and Extended Data Fig. 2).

We first confirmed using far-UV CD and NMR that the L- and D-peptides were disordered and enantiomeric (Fig. 3a–c and Extended

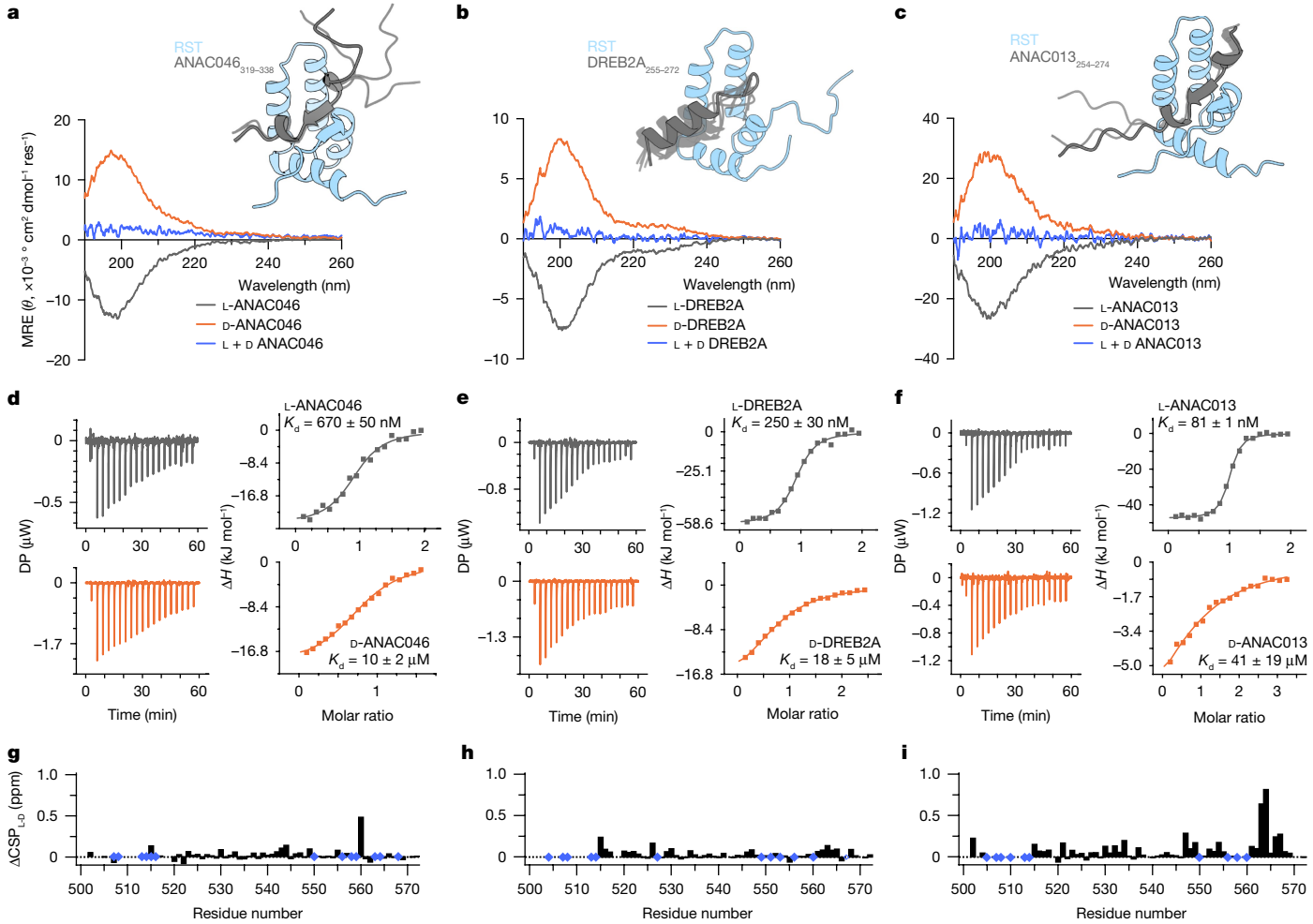

Fig. 3 | RST interactions with L- and D-peptides vary depending on remaining disorder in the complex. a–**c**, The peptides of ANAC046 (**a**), DREB2A (**b**) and ANAC013 (**c**) are disordered in their free state, and form varying structures upon binding to RST (top right). Far-UV CD spectra show the L- and D-enantiomers of each peptide as mirror images (sum of L- and D-peptide spectra is shown in blue). **d**–**f**, ITC for binding of 10–100 μM RST in the cell with 100–1,000 μM of ANAC046 (**d**), DREB2A (**e**) or ANAC013 (**f**) peptide in the syringe ($n = 3$, figure is representative). **g**–**i**, NMR CSPs of the interactions of RST with of ANAC046 (**g**), DREB2A (**h**) or ANAC013 (**i**) peptide showing the differences between the L- and D-enantiomers (>99% saturation, $n = 1$). Blue diamonds, indicate missing assignments, untraceable assigned residues or prolines.

Data Fig. 1). To determine the thermodynamics and the affinity of the interactions of L- or D-peptides with RST, we used ITC (Fig. 3d–f and Extended Data Table 2). We observed very different thermodynamic profiles for the three L-peptides, with more favourable enthalpy ($\Delta H°$) for DREB2A and ANAC013 than for ANAC046, whereas the opposite was the case for the entropy ($-T\Delta S°$), suggesting that the complexes had different characteristics. Comparing the effect of stereochemistry, we observed larger differences in K_d values as the interactions probably became more structured—that is, the difference between L-ANAC046 and D-ANAC046 was 15-fold (Fig. 3d), the difference between L-DREB2A and D-DREB2A was 72-fold (Fig. 3e) and the difference between L-ANAC013 and D-ANAC013 500-fold (Fig. 3f). The trend suggested that the amount of structure required for binding reduced the propensity of the D-enantiomer to interact with RST. This interpretation was further supported by comparing $\Delta CSP_{L\text{-}D}$ of RST induced by ANAC046 (Fig. 3g), DREB2A (Fig. 3h) and ANAC013 (Fig. 3i). The $\Delta CSP_{L\text{-}D}$ values of RST were substantial upon addition of ANAC013 and minimal upon addition of ANAC046. The same trend was observed in the pattern of peak intensity changes of RST (Extended Data Fig. 3), suggesting that ANAC046 is relatively disordered in complex with RST, whereas ANAC013 is more structured, and therefore less likely to interact with RST as a D-enantiomer. The $\Delta CSP_{L\text{-}D}$ values of RST for binding of DREB2A were between those for binding of ANAC046 and ANAC013, consistent with the differences in binding affinity for RST and effect of the D-enantiomer. Finally, we extracted K_d values and the dissociation rate constant (k_{off}) after fitting NMR titration data to a two-state model using NMR 2D lineshape analysis[31,32] (Extended Data Fig. 4), finding only minor effects of stereochemistry on the transition state energies (−2 to 1 kJ mol^{-1} ($\Delta\Delta G_{unbound\text{-}‡,D\text{-}L}$)) (Extended Data Fig. 5 and Extended Data Table 3). This observation highlights that the major effect of stereochemistry occurs after the transition state, in agreement with previous observations that native contacts consolidate late in the binding reaction pathway of IDPs[33–35].

In summary, it is apparent that the stereosensitivity of protein–protein interactions is not an all-or-none phenomenon, but instead occurs on a continuum. The results presented here indicate that sensitivity to chirality reflects the degree of disorder in the native complex.

To understand the sensitivity to chirality better, we investigated the RST complexes in more detail. We obtained insight into the RST-bound structures from C^{α} chemical shifts determined from chemical exchange saturation transfer (CEST) NMR for L-ANAC046 (Extended Data Fig. 6) and ZZ-exchange NMR for L-ANAC013 (Extended Data Fig. 7; 50% saturation), comparing them to similar available data for L-DREB2A[28]. A distinct pattern in structure emerges from the secondary chemical

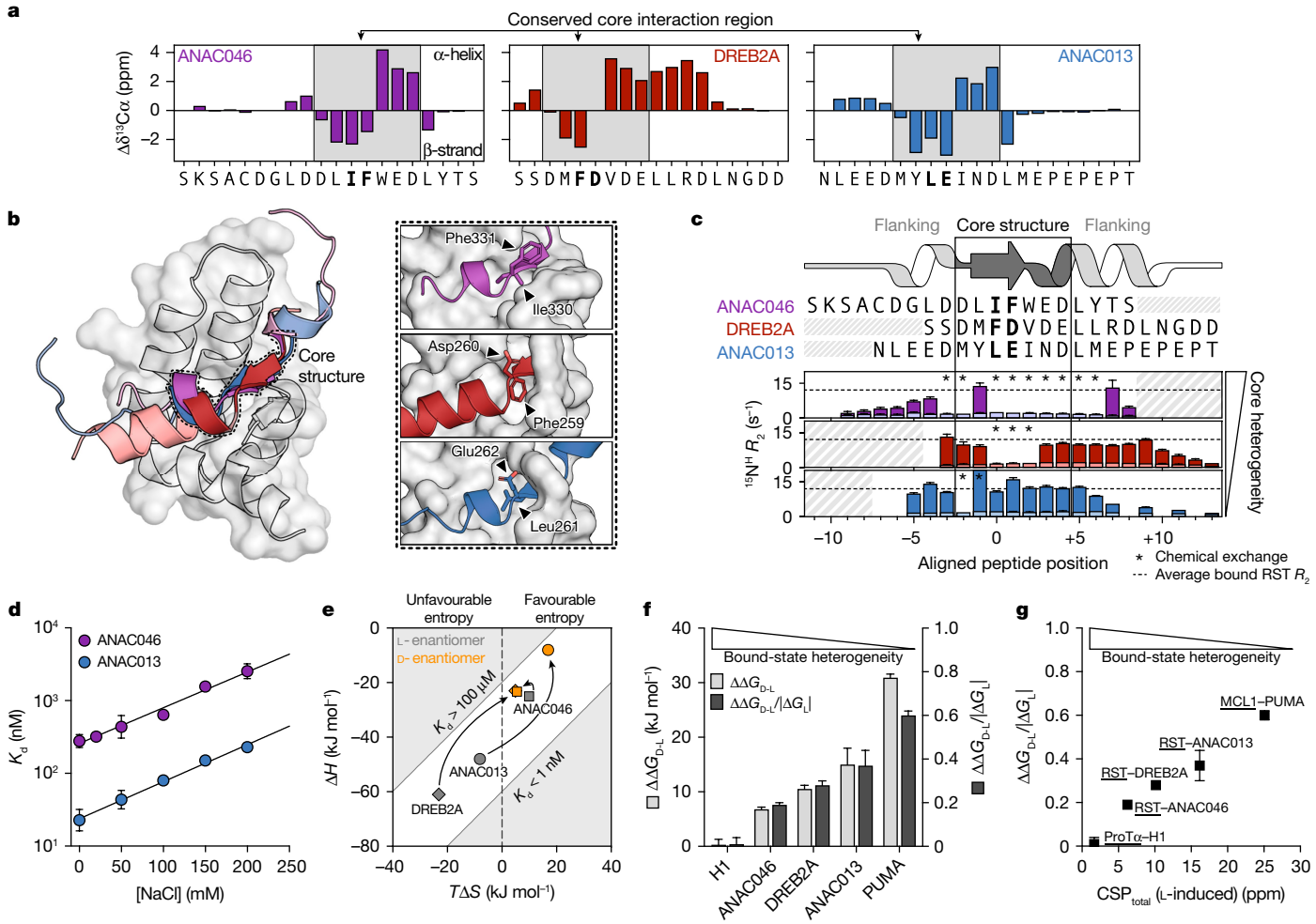

Fig. 4 | Ability to bind D-enantiomers scales with disorder of the complex. **a**, $^{13}C^{\alpha}$ SCS of L-enantiomers of ANAC046, DREB2A and ANAC013 in complex with RST. Four or more consecutive positive values indicate helical structure and three or more consecutive negative values indicate β-strand or extended structure. Grey regions highlight core structure. Key RST-interacting residues, shown as sticks in **b**, are highlighted in bold. **b**, Left, AlphaFold3-predicted structures of the RST complexes. Right, expanded view highlighting the binding sites, with interacting residues as sticks. **c**, Structure-based sequence alignment (top) and $^{15}N^{H}$ transverse relaxation rate constants (bottom) of free (light) and bound (dark) states of the RST-binding partners (error bars are standard errors of the fit). Asterisks indicate chemical exchange. The dashed line shows the outlier-excluded average R_2 value for free RST[28,50]. Possible structures formed are indicated by the top schematic and key RST-interacting residues, shown as sticks in **b**, are highlighted in bold. **d**, Ionic strength dependence of K_d value (error bars are s.d. from two technical replicates). The line is a linear fit of log(K_d) versus [NaCl] with concentrations varying from 10–30 μM RST in the cell and 100–300 μM peptide in the syringe ($n = 2$ except at 100 mM NaCl, where $n = 3$). **e**, Thermodynamic parameters of L- and D-enantiomer binding to RST. **f**, Stereosensitivity of the five model protein systems shown as the difference in ΔG ($\Delta\Delta G_{D\text{-}L}$, left y axis) and the fractional loss of binding energy ($\Delta\Delta G_{D\text{-}L}/|\Delta G_L|$, right y axis). **g**, Correlation between total CSP of the partner protein (ProTα, RST or MCL1) induced by L-enantiomer binding and the sensitivity to stereochemistry expressed as fractional loss of binding energy. In **f**,**g**, the wedge indicates the extent of bound-state heterogeneity and error bars were calculated from s.d. of ITC parameter shown in Extended Data Tables 2 and 3.

shifts (SCSs) (Fig. 4a). In their bound state, all three peptides have a similar core region comprising a short strand followed by a turn. Comparing the SCSs to the AlphaFold3-predicted structures of the complexes shows remarkable agreement between the NMR data and the predicted structures (Fig. 4a,b) unanimously suggesting the existence of a common structural core in all three bound RST partners. Aligning the peptides based on the core structure displaces the conserved Phe/Tyr residue of the sequence-based RST-binding motif[27] to align with an acidic and hydrophobic residue, respectively, suggesting that features beyond specific residue types are important (Fig. 4c). Indeed, all core structures are highly acidic and hydrophobic with a large and similar salt dependence in RST binding (Fig. 4d and data in ref. 36), further supporting the idea that binding of the core structure to RST is dependent on geometrically relaxed hydrophobic, ionic and π–cation interactions.

DREB2A and ANAC013 form additional structures in the core flanking regions, extending into a helix C-terminally (DREB2A) and forming a helical turn N-terminally (ANAC013) (Fig. 4a). This additional structuring was confirmed by the transverse relaxation rates (R_2 rates) obtained in the free and RST-bound states (Fig. 4c). In the bound states, DREB2A showed increased R_2 rates in the C-terminal flanking region, and ANAC013 increased R_2 rates in the N-terminal flanking region, compared with ANAC046 (Fig. 4c). Within the core structure, the number of residues exhibiting dynamics on an intermediate timescale originating from exchange between free and bound states or from heterogeneity in the bound state differed, as indicated by increased R_2 rates or missing signals. In complex with RST, ANAC046 showed increased dynamics in its core structure compared with that of DREB2A, which again was more dynamic than in ANAC013 (Fig. 4c). This observation provides an explanation for the observed variation in sensitivity to chirality,

suggesting that the RST complexes with greater bound-state dynamics are less sensitive to chirality.

The enthalpic and entropic contributions to binding provide insight into the interaction mechanisms[37,38] (Fig. 4e). For the RST complexes, a linear relationship between the changes in enthalpy and entropy is observed across the binding partners, with disordered and D-enantiomer interactions producing smaller changes and an entropic driving force (Fig. 4f). D-DREB2A and D-ANAC013 still bind and do so with an affinity and a thermodynamic profile analogous to those of L-ANAC046 and D-ANAC046. The thermodynamics of RST binding to L-ANAC046 and D-ANAC046 are similar, and in both cases, binding is driven by both entropy and enthalpy, highlighting a near independence from stereochemistry. Assuming that the interaction in these two cases mainly involves the core structure, this on its own has an affinity in the low micromolar range. As the thermodynamic profiles and the affinities for D-DREB2A and D-ANAC013 are similar to those for L-ANAC046 and D-ANAC046, their flanking regions are likely to engage very little with RST in the bound state (Fig. 4e). To assess the apparent graded response to chirality, we calculated for each binding pair the difference in ΔG between L- and D-peptides ($\Delta\Delta G_{D\text{-}L}$) and normalized the $\Delta\Delta G_{D\text{-}L}$ to the strength of the interaction by dividing by the Gibbs free energy of binding the L-enantiomer $|\Delta G_L|$ (Fig. 4f). There is no difference in these parameters between L-H1$_{155–175}$ and D-H1$_{155–175}$ interacting with ProTα, whereas interactions requiring backbone structuring show larger $\Delta\Delta G$ values, which increase when more backbone structure is formed. When optimal binding is independent of backbone folding, ambidextrous binding emerges, as for the RST:ANAC046 interaction and is most pronounced for the ProTα:H1 interaction. As more backbone folding occurs, as for the flanking regions of DREB2A and ANAC013 and for PUMA, the dynamics decreases and sensitivity towards chirality increases. Finally, focusing on the folded partner, we assessed the sensitivity to chirality across all systems. We correlated the total CSP induced by the L-enantiomer ($CSP_{total\text{–}L}$; Methods) to the stereosensitivity expressed by the fractional loss of binding energy ($\Delta\Delta G_{D\text{-}L}/|\Delta G_L|$). Although the CSP_{total_L} is a crude measure that depends, for example, on the size of the protein, the number of residues involved in binding, resolved peaks, dynamics, allostery and the chemistry, we observe a correlation between the NMR data for L-enantiomer binding and stereosensitivity (Fig. 4g). Thus, the larger the CSP_{total_L} of the folded partner, the greater the stereosensitivity.

In conclusion, the analyses of the RST complexes highlight that the propensity for interaction with a D-enantiomer, and thus the sensitivity towards chirality, depends on the extent of disorder and dynamics in the complex. Extending to the full set of five protein pairs, we find that CSPs of the binding partner could provide a method for predicting stereosensitivity.

Discussion

It is counterintuitive that an L-protein should be able to interact with a D-version of its natural partner. However, when considered further, we interrogated whether this applies to a truly disordered interaction. We find that protein complexes that are fully disordered (for example, ProTα:H1) form regardless of chirality. To our surprise, the observation was not limited to completely disordered polyelectrolyte binding partners. Instead, the propensity for interaction between L- and D-proteins exists on a continuum of disorder and order, irrespective of charge and hydrophobicity. The more disordered and dynamic the complex is, the less sensitive it is to chirality (Fig. 4 and Extended Data Table 1). These results, which were obtained from analyses of a set of five different complexes involving IDPs, provide an approach for assessing the degree of disorder within a protein complex directly from its sensitivity to chirality and vice versa. The approach is applicable not only in the case of a fully disordered complex driven by electrostatics, but also for complexes in which critical side chain interactions can be accommodated with adaptable and limited backbone structuring. This continuum of stereosensitivity has translational applications in drug design and implications for our understanding of protein evolution.

Chirality is an important feature for interactions that rely on structure or the formation of structure, but an electrostatic, disordered interaction can proceed regardless. Each of the peptides studied here relies on electrostatics to interact with their respective binding partner[24,28,39], therefore, the determining factor appears to be the degree of disorder. PUMA forms an encounter complex with MCL1 owing to long-range electrostatics[39], and electrostatics are also integral to the interactions of RST[28] (Fig. 4d). For the RST:ANAC046 complex, the interaction is achieved by arranging a few hydrophobic side chains, charges and π-electrons in a way that requires minimal backbone structuring of the core structure providing low sensitivity to chirality. Conversely, interactions of DREB2A and ANAC013 that rely on more extensive backbone folding have higher sensitivity to chirality. Thus, stereosensitivity appears to be rooted in backbone folding. Notably, adaptation of the associating folded partner also contributes to the sensitivity to chirality.

The central core structure, present in all tested RST partners, binds almost independently of chirality in a dynamic state driven by both entropy and enthalpy, while interactions of the flanking regions of the bound DREB2A and ANAC013 impose order, both to the core structure and to the flanking regions. Such strong enthalpy–entropy compensation within the core binding region imposed by dynamic flanking regions was reported previously for the N-terminal flanking region of DREB2A[40], and the larger enthalpic contribution for DREB2A binding shows that context matters[41].

In this study, we have investigated the disorder–order continuum of protein interactions with similar electrostatic and hydrophobic features (Extended Data Table 1). However, we do not know whether fully disordered hydrophobic complexes exist and whether they are sensitive to chirality, although hydrophobic ligands have been shown to remain disordered in complexes[42], and chaperones (such as GroEL/ES) can assist the folding of both L- and D-enantiomers[43]. Research into highly hydrophobic D-amino acid-based transcriptional coactivators has demonstrated that they can induce transcription to a similar level as their L-enantiomer counterparts[44], suggesting that at least some hydrophobic disordered proteins can still be functional regardless of chirality. An implication from our work is that such functional hydrophobic disordered complexes probably rely little on backbone folding. Thus, as IDPs have been historically difficult to target, requiring novel strategies[45,46], the presented results have substantial implications for the development of new, stable D-peptide drugs directed against IDPs.

Protein–protein interactions are fundamental for sustaining the information network that separates life from non-living systems. For simplicity, we assume that the quantities of abiotic amino acids of either chirality in the 'primordial soup' were equal[47]. Moreover, peptide bonds may form equally well between L-amino acids and D-amino acids, D-amino acids and D-amino acids, or L-amino acids and L-amino acids[48]. Therefore, peptide–peptide interactions between heterochiral peptides can be envisaged to have existed before biological systems became homochiral[49].

Online content

Any methods, additional references, Nature Portfolio reporting summaries, source data, extended data, supplementary information, acknowledgements, peer review information; details of author contributions and competing interests; and statements of data and code availability are available at https://doi.org/10.1038/s41586-024-08271-6.

1. Holehouse, A. S. & Kragelund, B. B. The molecular basis for cellular function of intrinsically disordered protein regions. *Nat. Rev. Mol. Cell Biol.* **25**, 187–211 (2024).
2. Mason, S. F. Origins of biomolecular handedness. *Nature* **311**, 19–23 (1984).

3. Silverman, M. P., Badoz, J. & Briat, B. Chiral reflection from a naturally optically active medium. *Opt. Lett.* **17**, 886 (1992).
4. Ikawa, M. & Snell, E. E. Cell wall composition of lactic acid bacteria. *J. Biol. Chem.* **235**, 1376–1382 (1960).
5. Ikawa, M. & Snell, E. E. D-glutamic acid and amino sugars as cell wall constituents in lactic acid bacteria. *Biochim. Biophys. Acta* **19**, 576–578 (1956).
6. Zhao, J. et al. EphA4 regulates hippocampal neural precursor proliferation in the adult mouse brain by D-serine modulation of *N*-methyl-D-aspartate receptor signaling. *Cereb. Cortex* **29**, 4381–4397 (2019).
7. Teramoto, T. et al. A novel peptide from funnel web spider venom, ω-Aga-TK, selectively blocks, P-type calcium channels. *Biochem. Biophys. Res. Commun.* **196**, 134–140 (1993).
8. Mignogna, G., Simmaco, M., Kreil, G. & Barra, D. Antibacterial and haemolytic peptides containing D-alloisoleucine from the skin of *Bombina variegata*. *EMBO J.* **12**, 4829–4832 (1993).
9. Martínez-Rodríguez, S., Martínez-Gómez, A. I., Rodríguez-Vico, F., Clemente-Jiménez, J. M. & Las Heras-Vázquez, F. J. Natural occurrence and industrial applications of D-amino acids: an overview. *Chem. Biodivers.* **7**, 1531–1548 (2010).
10. Tugyi, R. et al. Partial D-amino acid substitution: Improved enzymatic stability and preserved Ab recognition of a MUC2 epitope peptide. *Proc. Natl Acad. Sci. USA* **102**, 413–418 (2005).
11. Schumacher, T. N. et al. Identification of D-peptide ligands through mirror-image phage display. *Science* **271**, 1854–1857 (1996).
12. Sun, K. et al. Accurate de novo design of heterochiral protein–protein interactions. *Cell Res.* https://doi.org/10.1038/s41422-024-01014-2 (2024).
13. Doti, N., Mardirossian, M., Sandomenico, A., Ruvo, M. & Caporale, A. Recent applications of retro-inverso peptides. *Int. J. Mol. Sci.* **22**, 8677 (2021).
14. Lombardi, A. et al. Retro-inverso D-peptides as a novel targeted immunotherapy for type 1 diabetes. *J. Autoimmun.* **115**, 102543 (2020).
15. Bonny, C., Oberson, A., Negri, S., Sauser, C. & Schorderet, D. F. Cell-permeable peptide inhibitors of JNK: novel blockers of beta-cell death. *Diabetes* **50**, 77–82 (2001).
16. Shangary, S. & Wang, S. Targeting the MDM2–p53 interaction for cancer therapy. *Clin. Cancer Res.* **14**, 5318 (2008).
17. Beydoun, T. et al. Subconjunctival injection of XG-102, a JNK inhibitor peptide, in patients with intraocular inflammation: a safety and tolerability study. *J. Ocul. Pharmacol. Ther.* **31**, 93–99 (2015).
18. Mao, A. H., Crick, S. L., Vitalis, A., Chicoine, C. L. & Pappu, R. V. Net charge per residue modulates conformational ensembles of intrinsically disordered proteins. *Proc. Natl Acad. Sci. USA* **107**, 8183–8188 (2010).
19. Wright, P. E. & Dyson, H. J. Intrinsically disordered proteins in cellular signalling and regulation. *Nat. Rev. Mol. Cell Biol.* **16**, 18–29 (2015).
20. van der Lee, R. et al. Classification of intrinsically disordered regions and proteins. *Chem. Rev.* **114**, 6589–6631 (2014).
21. Tuttle, L. M. et al. Gcn4-mediator specificity is mediated by a large and dynamic fuzzy protein–protein complex. *Cell Rep.* **22**, 3251–3264 (2018).
22. Borgia, A. et al. Extreme disorder in an ultrahigh-affinity protein complex. *Nature* **555**, 61–66 (2018).
23. Turner, A. L. et al. Highly disordered histone H1–DNA model complexes and their condensates. *Proc. Natl Acad. Sci. USA* **115**, 11964–11969 (2018).
24. Sottini, A. et al. Polyelectrolyte interactions enable rapid association and dissociation in high-affinity disordered protein complexes. *Nat. Commun.* **11**, 5736 (2020).
25. Day, C. L. et al. Structure of the BH3 domains from the p53-inducible BH3-only proteins Noxa and Puma in complex with Mcl-1. *J. Mol. Biol.* **380**, 958–971 (2008).
26. Rogers, J. M. et al. Interplay between partner and ligand facilitates the folding and binding of an intrinsically disordered protein. *Proc. Natl Acad. Sci. USA* **111**, 15420–15425 (2014).
27. O'Shea, C. et al. Structures and short linear motif of disordered transcription factor regions provide clues to the interactome of the cellular hub protein radical-induced cell death 1. *J. Biol. Chem.* **292**, 512–527 (2017).
28. Bugge, K. et al. Structure of radical-induced cell death1 hub domain reveals a common αα-scaffold for disorder in transcriptional networks. *Structure* **26**, 734–746.e7 (2018).
29. Mirdita, M. et al. ColabFold: making protein folding accessible to all. *Nat. Methods* **19**, 679–682 (2022).
30. Abramson, J. et al. Accurate structure prediction of biomolecular interactions with AlphaFold 3. *Nature* **630**, 493–500 (2024).
31. Waudby, C. A., Ramos, A., Cabrita, L. D. & Christodoulou, J. Two-dimensional NMR lineshape analysis. *Sci. Rep.* **6**, 24826 (2016).
32. Waudby, C. A. & Christodoulou, J. NMR lineshape analysis of intrinsically disordered protein interactions. *Methods Mol. Biol.* **2141**, 477–504 (2020).
33. Haq, S. R. et al. Side-chain interactions form late and cooperatively in the binding reaction between disordered peptides and PDZ domains. *J. Am. Chem. Soc.* **134**, 599–605 (2012).
34. Gianni, S., Morrone, A., Giri, R. & Brunori, M. A folding-after-binding mechanism describes the recognition between the transactivation domain of c-Myb and the KIX domain of the CREB-binding protein. *Biochem. Biophys. Res. Commun.* **428**, 205–209 (2012).
35. Dogan, J., Mu, X., Engström, Å. & Jemth, P. The transition state structure for coupled binding and folding of disordered protein domains. *Sci. Rep.* **3**, 2076 (2013).
36. Elkjær, S. et al. Evolutionary fine-tuning of residual helix structure in disordered proteins manifests in complex structure and lifetime. *Commun. Biol.* **6**, 63 (2023).
37. Teilum, K., Olsen, J. G. & Kragelund, B. B. Globular and disordered-the non-identical twins in protein–protein interactions. *Front. Mol. Biosci.* **2**, 40 (2015).
38. Skriver, K., Theisen, F. F. & Kragelund, B. B. Conformational entropy in molecular recognition of intrinsically disordered proteins. *Curr. Opin. Struct. Biol.* **83**, 102697 (2023).
39. Chu, W. T., Clarke, J., Shammas, S. L. & Wang, J. Role of non-native electrostatic interactions in the coupled folding and binding of PUMA with Mcl-1. *PLoS Comput. Biol.* **13**, e1005468 (2017).
40. Theisen, F. F. et al. Quantification of conformational entropy unravels effect of disordered flanking region in coupled folding and binding. *J. Am. Chem. Soc.* **143**, 14540–14550 (2021).
41. Bugge, K. et al. Interactions by disorder—a matter of context. *Front. Mol. Biosci.* **7**, 110 (2020).
42. Wiggers, F. et al. Diffusion of a disordered protein on its folded ligand. *Proc. Natl Acad. Sci. USA* **118**, e2106690118 (2021).
43. Weinstock, M. T., Jacobsen, M. T. & Kay, M. S. Synthesis and folding of a mirror-image enzyme reveals ambidextrous chaperone activity. *Proc. Natl Acad. Sci. USA* **111**, 11679–11684 (2014).
44. Nyanguile, O., Uesugi, M., Austin, D. J. & Verdine, G. L. A nonnatural transcriptional coactivator. *Proc. Natl Acad. Sci. USA* **94**, 13402–13406 (1997).
45. Heller, G. T. et al. Small-molecule sequestration of amyloid-β as a drug discovery strategy for Alzheimer's disease. *Sci. Adv.* **6**, eabb5924 (2020).
46. Iconaru, L. I. et al. Small molecule sequestration of the intrinsically disordered protein, p27Kip1, within soluble oligomers. *J. Mol. Biol.* **433**, 167120 (2021).
47. Sallembien, Q., Bouteiller, L., Crassous, J. & Raynal, M. Possible chemical and physical scenarios towards biological homochirality. *Chem. Soc. Rev.* **51**, 351–368 (2022).
48. James, E. J. & Russell, M. J. Predicting the conformations of peptides and proteins in early evolution. *Biol. Direct* **3**, 3 (2008).
49. Milner-White, E. J. & Russell, M. J. Functional capabilities of the earliest peptides and the emergence of life. *Genes* **2**, 671–688 (2011).
50. Staby, L. et al. Flanking disorder of the folded αα-hub domain from radical induced cell death1 affects transcription factor binding by ensemble redistribution. *J. Mol. Biol.* **433**, 167320 (2021).

Methods

Synthetic peptides

Synthetic L- and D-peptides of $H1_{155–175}$, $PUMA_{130–156}$, $ANAC013_{254–274}$, $ANAC046_{319–338}$ and $DREB2A_{255–272}$ were purchased from Pepscan (now Biosynth) at a minimum purity of 95% and purified by HPLC. The D-peptides contain amino acid residues with a stereoisomeric D-form of each chiral carbon. The peptides were either resuspended in MilliQ H_2O or in MilliQ H_2O containing 50 mM NH_4HCO_3 and lyophilized repeatedly to remove leftover trifluoroacetic acid from the last purification step by the manufacturer. Peptides were then either resuspended directly in the buffer used for experiments or in H_2O without 50 mM NH_4HCO_3 to measure the concentration. If no aromatic residue was present in the peptide sequence, the absorbance at 214 nm was used. The extinction coefficient was calculated using Bestsel[51].

Expression and purification of proteins

^{15}N-labelled and unlabelled full-length ProTα was expressed and purified as described[22]. The double-cysteine variant of ProTα (E56C/D110C) used in smFRET experiments was expressed and purified as described[24], with some modifications. In brief, ProTα was dialysed against Tris buffer (50 mM Tris, 200 mM NaCl, 2 mM DTT, 1 mM EDTA; pH 8), during which the hexa-histidine tag was cleaved using HRV 3 C protease. Cleaved ProTα was purified further using Ni Sepharose Excel resin (Cytiva, formerly GE Healthcare) and a HiPrep Q FF column (Cytiva) with a gradient from 200 mM to 1 M NaCl. Buffer was exchanged (HiTrap Desalting column (Cytiva)) to labelling buffer potassium phosphate (100 mM, pH 7). ^{15}N-labelled and unlabelled GST–$MCL1_{152–308}$ was expressed in BL21(DE3)pLysS *Escherichia coli* in the presence of ampicillin. Cells were grown at 37 °C in LB or M9 minimal medium (for ^{15}N labelling) until OD_{600} reached 0.6, then induced with IPTG (1 mM final concentration) and collected after 4 h. The cell pellet was resuspended in Tris buffer (20 mM Tris, 100 mM NaCl; pH 8), then lysed by sonication. After pelleting again, the supernatant was applied to GST Sepharose beads (Cytiva), and GST–$MCL1_{152-308}$ was eluted using Tris-GSH buffer (20 mM Tris, 100 mM NaCl, 10 mM GSH; pH 8). The GST tag was removed using TEV protease (0.7 mg) overnight at room temperature. Final purity was reached using a Superdex 75 26/60 column (Cytiva), equilibrated with 50 mM phosphate buffer (pH 7). ^{13}C,^{15}N-labelled $MCL1_{152–308}$ was expressed as described[52] and purified as above. The expression and purification of ^{15}N-labelled and unlabelled RCD1-$RST_{499–572}$ were carried out as previously described[28] with the lysis buffer changed to 20 mM Tris-HCl, pH 9.0, 20 mM NaCl. The buffer used in the last purification step by size exclusion chromatography on a Superdex 75 10/300 GL column (Cytiva) was the buffer described for the individual methods.

^{13}C,^{15}N-labelled $ANAC046_{319–338}$ or $ANAC013_{254–274}$ were expressed with a His_6-SUMO fusion tag in BL21(DE3) *E. coli* in the presence of kanamycin (50 μg ml^{-1}). Cells were grown in LB at 37 °C until OD_{600} reached 0.6 and the medium was changed to M9 minimal medium, followed by induction with IPTG to 1 mM final concentration and collected after incubation overnight at 16 °C. The cells were resuspended in lysate buffer (50 mM and 20 mM Tris-HCl for $ANAC046_{319–338}$ and $ANAC013_{254–274}$, respectively, pH 8.0, 300 mM NaCl) and sonicated. After the centrifugation, the lysate was purified using TALON resin equilibrated in the buffers just described. The fusion peptides were eluted with an equivalent buffer containing 250 mM imidazole. After a dialysis step into 20 mM Tris-HCl pH 8.0, 100 mM NaCl, the fusion tag was cleaved with ubiquitin-like-specific protease 1 (ULP1) (molar ratio between peptide and protease were 1:320 and 1:500 for $ANAC046_{319–338}$ and $ANAC013_{254–274}$, respectively) overnight at 4 °C. A second purification step with TALON resin was performed resulting in the peptides in the flowthrough. The purification of the peptides was finalized by size exclusion chromatography on a Superdex peptide 10/300 GL column (Cytiva) and freeze-dried to be resuspended in the desired buffer.

AlphaFold structure modelling

Protein interaction models of RCD1-$RST_{499–572}$ in complex with $ANAC046_{319–338}$ or $ANAC013_{254–274}$ were generated using AlphaFold3[30] and analysed in PyMOL (The PyMOL Molecular Graphics System, version 3.0 Schrödinger, LLC.). The five generated models for each complex were assessed manually and compared with the secondary chemical shifts of C^{α} of the L-ligand recorded using ZZ-exchange or CEST (see NMR spectroscopy method). The structures agreeing with the experimental data were visualized in PyMOL or Chimera X[53].

Far-UV CD spectropolarimetry

Far-UV CD spectra of L- and D-peptides of $H1_{155–175}$, $PUMA_{130–156}$, $ANAC013_{254–274}$, $ANAC046_{319–338}$, and $DREB2A_{255–272}$ were measured on a Jasco 815 spectropolarimeter with a Jasco Peltier control in the range of 260–190 nm at 20 °C. Concentrations of peptides varied between 10–30 μM in either MilliQ H_2O, pH 7.0 ($PUMA_{130–156}$, $H1_{155–175}$) or 20 mM NaH_2PO_4/Na_2HPO_4, pH 7.0 ($ANAC013_{254–274}$, $ANAC046_{319–338}$, $DREB2A_{255–272}$) with 1 mM TCEP in the samples containing ANAC046 peptides. A quartz cuvette with a 1 mm path length was used and 10 scans were recorded and averaged with a scanning speed of 20 nm min^{-1} and response time of 2 s. A spectrum of the buffer using identical setting was recorded for each protein and subtracted the sample spectrum.

NMR spectroscopy

All NMR spectra were recorded on Bruker Avance III 600 MHz, 750 MHz or an Avance NEO 800 MHz (for ^{1}H) spectrometers equipped with cryoprobes. Natural abundance ^{1}H,^{15}N and ^{1}H,^{13}C-HSQC spectra were recorded on all peptides at either 10 °C or 25 °C. Peptides (0.5 mM) in sample buffer containing 20 mM Na_2HPO_4/NaH_2PO_4 pH 7.0, 100 mM NaCl, 10 % (v/v) D_2O, 0.02 % (w/v) NaN_3 and 0.7 mM 4,4-dimethyl-4-silapentane-1-sulfonic acid (DSS) for $ANAC046_{319–338}$, $ANAC013_{254–274}$ and $DREB2A_{255–272}$ with the addition of 1 mM DTT in the samples containing ANAC046 peptides. ^{1}H,^{15}N-HSQC spectra were recorded on 50 μM ProTα, with or without 500 μM L- or D-$H1_{155–175}$ in TBSK (ionic strength 165 mM; pH 7.4). ^{1}H,^{15}N-HSQC spectra were recorded on 50 μM MCL1, with or without 45 μM L- or 2.5 mM D-$PUMA_{130–156}$, in Tris (50 mM; pH 7.0) to compare at 90% saturation, as calculated from K_d values. Assignments of ^{13}C,^{15}N-MCL1 in complex with L-$PUMA_{130–156}$ were completed from a series of HNCACB and HNCOCACB 3D spectra as described[54], and deposited to Biological Magnetic Resonance Data Bank (BMRB) under accession 52264. ^{1}H,^{15}N-HSQC spectra were recorded on ^{15}N-labelled 100 μM RCD1-$RST_{499–572}$ in 20 mM Na_2HPO_4/NaH_2PO_4 pH 7.0, 100 mM NaCl, 10 % (v/v) D_2O, 0.02 % (w/v) NaN_3 and 0.7 mM DSS at 25 °C in the absence and presence of each stereoisomeric forms of 0–200 μM $ANAC046_{319–338}$, $ANAC013_{254–274}$ and $DREB2A_{255–272}$ in the following ratios; 1:0, 1:0.2, 1:0.4, 1:0.6, 1:0.8, 1:1 and 1:2. Assignments of free ProTα and free RCD1-RST were taken from BMRB entries 27215 and 50545, respectively[22,28].

Amide CSPs were calculated from the ^{1}H,^{15}N-HSQCs in the absence and presence of the highest concentration of peptide used for each interaction using equation (1):

$$\Delta\delta_{NH}\,(\text{ppm}) = \sqrt{(\Delta\delta^{1}\text{H})^2 + (0.154 \times \Delta\delta^{15}\text{N})^2} \qquad (1)$$

The total protein CSP (CSP_{total_L}) induced by the binding of the L-enantiomer peptide was quantified by recording the CSPs of all visible ^{15}N,$^1H^N$ backbone resonances at >90% saturation (MCL1: 90%, RST (all cases): >99%, ProTα: >98%). The CSP for all visible residues were summed to obtain the total CSP. To adjust for unassigned residues, which include prolines, residues that could not be assigned, or residues not visible in either the bound or unbound states, the total CSP was divided by the fraction of residues for which CSPs were recorded. For instance, if CSPs were obtained for only half of the residues, the calculated total CSP was doubled to estimate the perturbation as

if all residues were visible. This adjustment ensured that the total CSP could be compared between interactions, accounting for the lack of data from unassigned or invisible residues. The adjustment does not account for the fact that disappearing residues are likely involved in the interaction and thus also likely to experience larger than average CSPs.

2D NMR lineshape analysis. 2D NMR lineshape analyses were performed for interactions of L-and D-peptides with RCD1-RST$_{499-572}$. The recorded ^{1}H,^{15}N-HSQC spectra were processed using qMDD with exponential weighting functions with 4 Hz and 8 Hz line broadening in the direct and indirect dimensions, respectively. The 2D lineshape analysis was performed using the tool TITAN[31] in Matlab (Mathworks) and was based on well-separated spin systems that were easily followed. If the trajectory of spin systems overlapped, the spin systems were grouped during fitting. All titrations were fitted to a two-state binding model, and at least 12 spin systems were picked for each analysis. Due to initial poor fitting for the titrations of the interaction ^{15}N-RCD1-RST$_{499-572}$ and L- ANAC013$_{254-274}$, the K_d value was fixed using the values determined from ITC. Errors were determined by a bootstrap analysis using 100 replicas to determine the standard error from the mean. From the lineshape analysis, the fitted K_d and k_{off} values were used to calculate the association rate constant (k_{on}) based on equation (2):

$$K_d = \frac{k_{off}}{k_{on}} \quad (2)$$

The differences in activation free energies for binding between D- and L-peptides were estimated from the ratios of the association rate constants for both stereoisomers, k_{on}^{D} and k_{on}^{L}, based on equation (3):

$$\Delta\Delta G_{unbound-\ddagger,D-L} = RT\ln\left(\frac{k_{on}^{L}}{k_{on}^{D}}\right), \quad (3)$$

which was rewritten from Fersht (equation 18.22 in ref. 55).

CEST NMR. CEST experiments were recorded for the L-peptide of ANAC046$_{319-338}$ to determine the chemical shift of its bound state with RCD1-RST$_{499-572}$. All experiments were recorded on a Bruker Avance Neo 800 spectrometer with a cryoprobe. A sample of 1 mM ^{13}C,^{15}N-labelled L-ANAC046$_{319-338}$ was prepared with 5% molar ratio of RCD1-RST$_{499-572}$ in 20 mM Na_2HPO_4/NaH_2PO_4 pH 6.5, 100 mM NaCl, 10 % (v/v) D_2O, 0.02 % (w/v) NaN_3, 0.7 mM DSS and 5 mM DTT. ^{15}N-CEST data was acquired using pulse sequences as previously described[56] at 25 °C using three different $\mathbf{B}_1$ field strengths: 6.25, 12.5 and 25 Hz. ^{13}C-CEST data were acquired using special pulse sequences[57,58] (provided by L. Kay) as done in ref. 59 at 25 °C with a $\mathbf{B}_1$ field strength of 25 Hz. The free induction decays were transformed using NMRPipe[60] and peak intensities were extracted from each specific peak position. The intensities were analysed using ChemEx[61] by fitting to a global two-state model implemented in the program. The fits reported on the change in chemical shifts for peaks experiencing CEST-transfer which directly reflects the chemical shift of the bound state of the peptide. The chemical shifts were extracted for the C$^{\alpha}$ and compared to a reference set[62].

ZZ-exchange. For the complex between RST and ^{15}N-ANAC013$_{254-274}$, identification of residues and their assignments were resolved by 3D heteronuclear NMR experiments with additional ZZ-exchange[63] NMR spectra recorded on a 50% saturated sample of 100 µM ^{13}C, ^{15}N-ANAC013$_{254-274}$ with 50 µM RCD1-RST$_{499-572}$ in20 mM Na_2HPO_4/NaH_2PO_4 pH 6.5, 200 mM NaCl, 10 % (v/v) D_2O, 0.02 % (w/v) NaN_3, and 0.7 mM DSS. The ZZ-exchange connections made it possible to manually track the assignment from the ^{1}H,^{15}N-HSQC spectrum of the unbound ^{15}N-ANAC013$_{254-274}$ to the RST-bound ^{15}N-ANAC013$_{254-274}$. For the assignments of carbon resonances of ANAC013, two samples were prepared: ^{13}C, ^{15}N-ANAC013$_{254-274}$ (650 µM) w/wo RCD1-RST$_{499-572}$ (800 µM) in 20 mM Na_2HPO_4/NaH_2PO_4 pH 6.5, 200 mM NaCl, 10 % (v/v) D_2O, 0.02 % (w/v) NaN_3, and 0.7 mM DSS. Backbone resonances for the unbound peptide were manually assigned from analysis of ^{15}N-HSQC, HNCA, HNCO and HNCACB experiments. All NMR spectra were acquired at 25 °C on a Bruker Avance III 750 MHz, except for ZZ-exchange which was on Bruker Avance III 600 MHz. All 3D experiments were recorded using non-uniform sampling.

Secondary chemical shifts. SCSs were calculated using the POTENCI[62] web tool.

Transverse relaxation. To determine the dynamics of L-ANAC046$_{319-338}$ and L-ANAC013$_{254-274}$ w/wo RCD1-RST$_{499-572}$, the sample from ANAC013$_{254-274}$ assignment was reused whereas a new for ANAC046$_{319-338}$ was made: 75 µM ^{13}C, ^{15}N-ANAC046$_{319-338}$ with 180 µM RCD1-RST$_{499-572}$ in 20 mM Na_2HPO_4/NaH_2PO_4 pH 6.5, 100 mM NaCl, 10 % (v/v) D_2O, 0.02 % (w/v) NaN_3, 0.7 mM DSS and 5 mM DTT. The transverse relaxation rates, R_2 values, were acquired on a Bruker Avance Neo 800 spectrometer with the following relaxation delays: 33.8 ms, 67.6 ms, 101.4 ms, 169.0 ms, 236.6 ms, 270.4 ms, 338.0 ms and 405.6 ms (all triplicates), and a recycle delay of 2 s. Data were fitted to a one phase decay function.

Isothermal titration calorimetry

Prior to ITC, all samples were spun down at 17,000*g* for 10 min at the experimental temperature. ITC experiments involving ProTα and MCL1$_{152-308}$ as interaction partners were recorded on MicroCal PEAQ-ITC microcalorimeter (Malvern Panalytical). ProTα (7.1 µM) was placed in the cell and either L- or D-H1$_{155-175}$ (99.1 µM) in the syringe, in TBSK (165 µM ionic strength) at 20 °C. Each injection was 2 µl, with a total of 19 injections at an interval of 150 s between each. Data were fit using a fixed number of binding sites (fixed to one) so that fits could be standardized. For the MCL1$_{152-308}$ interactions, MCL1$_{152-308}$ (10 µM) was placed in the cell, with either L- or D-PUMA$_{130-156}$ (100 µM) in the syringe, in Tris (50 mM; pH 7.0) at 25 °C. Each of the 35 injections was 1 µl, with an interval of 150 s between each. The experiment was repeated for MCL1:D-PUMA$_{130-156}$, increasing the concentrations to 70 and 700 µM, respectively, while keeping the remaining experimental conditions identical. ITC experiments involving RCD1-RST$_{499-572}$ as interaction partner were recorded on a MicroCal ITC$_{200}$ microcalorimeter (MicroCal Instruments) at 25 °C in 50 mM Na_2HPO_4/NaH_2PO_4 pH 7.0, 100 mM NaCl. TCEP (1 mM) was added the sample buffer for interactions involving ANAC046 peptides. Concentrations of RCD1-RST$_{499-572}$ varied between 10–100 µM in the cell and 100-1000 µM of the ANAC046, ANAC013 or DREB2A peptides in the syringe. The first injection was 0.5 µl followed by 18 repetitions of 2 µl injections separated by 180 seconds. These experiments were processed using the Origin7 software package supplied by the manufacturer. The last 18 injections of each experiment were fitted to a one set of sites binding model. Triplicates were recorded for each interaction.

A salt titration was performed measuring the interaction between RCD1-RST$_{499-572}$ and the L-peptides of ANAC046$_{319-338}$ and ANAC013$_{254-274}$ by ITC, varying the NaCl concentration in the experimental buffer. Experiments were recorded on a MicroCal PEAQ-ITC microcalorimeter or a MicroCal ITC200 microcalorimeter at 25 °C. A 50 mM Na_2HPO_4/NaH_2PO_4 pH 7.0, 1 mM TCEP buffer was used with NaCl concentrations at 0, 50, 150 and 200 mM, with data at 100 mM NaCl recorded prior to and included in the analysis. Protein and peptide concentrations varied from 10–30 µM in the cell (RCD1-RST) and 100–300 µM in the syringe (peptides). A replica of each experiment was produced, and the isotherm were fitted as described above.

Fluorophore labelling for smFRET

ProTα was labelled by incubating it with Alexa Fluor 488 (0.7:1 dye to protein molar ratio) for 1 h at room temperature and sequentially

with Alexa Fluor 594 (1.5:1 dye to protein molar ratio) overnight at 4 °C. Labelled protein was purified using a HiTrap Desalting column and reversed-phase high-performance liquid chromatography (RP-HPLC) on a SunFire C18 column (Waters Corporation) with an elution gradient from 20% acetonitrile and 0.1% trifluoroacetic acid in aqueous solution to 37% acetonitrile. ProTα-containing fractions were lyophilized and dissolved in buffer (10 mM Tris, 200 mM KCl, 1 mM EDTA; pH 7.4).

Single-molecule FRET measurements and analysis

Single-molecule fluorescence experiments were conducted using either a custom-built confocal microscope or a MicroTime 200 confocal microscope (PicoQuant) equipped with a 485-nm diode laser and an Olympus UplanApo 60×/1.20 W objective. Microscope and filter setup were used as previously described[24]. The 485-nm diode laser was set to an average power of 100 µW (measured at the back aperture of the objective), either in continuous-wave or pulsed mode with alternating excitation of the dyes, achieved using pulsed interleaved excitation (PIE)[64]. The wavelength range used for acceptor excitation in PIE mode was selected with a z582/15 band pass filter (Chroma) from the emission of a supercontinuum laser (EXW-12 SuperK Extreme, NKT Photonics) driven at 20 MHz, which triggers interleaved pulses from the 485-nm diode laser used for donor excitation. In our experiments, photon bursts (at least 3000 bursts) were selected against the background mean fluorescence counts and, in case of PIE, by having a stoichiometry ratio S of $0.2 < S < 0.75$, each originating from an individual molecule diffusing through the confocal volume. Transfer efficiencies were quantified according to $E = n_A/(n_A + n_D)$, where n_D and n_A are the numbers of donor and acceptor photons in each burst, respectively, corrected for background, channel crosstalk, acceptor direct excitation, differences in quantum yields of the dyes, and detection efficiencies. All smFRET experiments were performed in µ-Slide sample chambers (Ibidi) at 22 °C in TEK buffer with an ionic strength of 165 mM fixed with KCl; 140 mM 2-mercaptoethanol and 0.01% (v/v) Tween-20 were added for photoprotection and for minimizing surface adhesion, respectively. Single-molecule data were analysed using the Mathematica (Wolfram Research) package Fretica (https://schuler.bioc.uzh.ch/programs). For quantifying binding affinities, transfer efficiency histograms were constructed from single-molecule photon bursts identified as described above. Each histogram was normalized to an area of 1 and fit with a Gaussian peak function to extract its mean transfer efficiency $\langle E \rangle$. The mean transfer efficiency as a function of increasing concentration of D/L-H1$_{155–175}$, $\langle E \rangle(C_{D/L-H1})$, was fit with:

$$\langle E \rangle(C^{tot}_{D/L-H1}) = \Delta\langle E \rangle^{sat} \times \frac{C^{tot}_{D/L-H1} + K_d + C^{tot}_{ProT\alpha} - \sqrt{(C^{tot}_{D/L-H1} + K_d + C^{tot}_{ProT\alpha})^2 - 4C^{tot}_{D/L-H1}C^{tot}_{ProT\alpha}}}{2C^{tot}_{ProT\alpha}} + \langle E \rangle_0 \quad (4)$$

Here, $C^{tot}_{D/L-H1}$ and $C^{tot}_{ProT\alpha}$ are the total concentration of D/L-H1$_{155–175}$ and ProTα, respectively, $\langle E \rangle_0$ is the mean transfer efficiency of free ProTα, and $\Delta\langle E \rangle^{sat}$ is the increase in transfer efficiency from free ProTα to ProTα saturated with D/L-H1$_{155–175}$, while K_d is the equilibrium dissociation constant.

Reporting summary

Further information on research design is available in the Nature Portfolio Reporting Summary linked to this article.

Data availability

Chemical shifts of MCL1 in the PUMA-bound state have been submitted to BMRB under the accession number 52264. Source data are provided with this paper.

51. Kuipers, B. J. H. & Gruppen, H. Prediction of molar extinction coefficients of proteins and peptides using UV absorption of the constituent amino acids at 214 nm to enable quantitative reverse phase high-performance liquid chromatography-mass spectrometry analysis. *J. Agric. Food Chem.* **55**, 5445–5451 (2007).
52. Newcombe, E. A. et al. Insight into calcium-binding motifs of intrinsically disordered proteins. *Biomolecules* **11**, 1173 (2021).
53. Meng, E. C. et al. UCSF ChimeraX: tools for structure building and analysis. *Protein Sci.* **32**, e4792 (2023).
54. Schenstrøm, S. M. et al. Expanded interactome of the intrinsically disordered protein Dss1. *Cell Rep.* **25**, 862–870 (2018).
55. Fersht, A. *Structure and Mechanism in Protein Science: A Guide to Enzyme Catalysis and Protein Folding*, 3rd edn (W. H. Freeman, 1998).
56. Vallurupalli, P., Bouvignies, G. & Kay, L. E. Studying 'invisible' excited protein states in slow exchange with a major state conformation. *J. Am. Chem. Soc.* **134**, 8148–8161 (2012).
57. Long, D., Sekhar, A. & Kay, L. E. Triple resonance-based $^{13}C^{\alpha}$ and $^{13}C^{\beta}$ CEST experiments for studies of ms timescale dynamics in proteins. *J. Biomol. NMR* **60**, 203–208 (2014).
58. Vallurupalli, P. & Kay, L. E. Probing slow chemical exchange at carbonyl sites in proteins by chemical exchange saturation transfer NMR spectroscopy. *Angew. Chem. Int. Ed. Engl.* **52**, 4156–4159 (2013).
59. Theisen, F. F. et al. Molecular switching in transcription through splicing and proline-isomerization regulates stress responses in plants. *Nat. Commun.* **15**, 592 (2024).
60. Delaglio, F. et al. NMRPipe: a multidimensional spectral processing system based on UNIX pipes. *J. Biomol. NMR* **6**, 277–293 (1995).
61. Bouvignies, G. NMR chemical exchange analysis tool. *Github* https://www.github.com/gbouvignies/ChemEx (2022).
62. Nielsen, J. T. & Mulder, F. A. A. POTENCI: prediction of temperature, neighbor and pH-corrected chemical shifts for intrinsically disordered proteins. *J. Biomol. NMR* **70**, 141–165 (2018).
63. Palmer, A. G., Kroenke, C. D. & Loria, J. P. Nuclear magnetic resonance methods for quantifying microsecond-to-millisecond motions in biological macromolecules. *Methods Enzymol.* **339**, 204–238 (2001).
64. Müller, B. K., Zaychikov, E., Bräuchle, C. & Lamb, D. C. Pulsed interleaved excitation. *Biophys. J.* **89**, 3508–3522 (2005).
65. Holehouse, A. S., Das, R. K., Ahad, J. N., Richardson, M. O. G. & Pappu, R. V. CIDER: resources to analyze sequence–ensemble relationships of intrinsically disordered proteins. *Biophys. J.* **112**, 16–21 (2017).

Acknowledgements The authors thank K. Strømgaard for valuable discussions on D-peptide synthesis; C. B. Parsbæk for initial discussions on the MCL1–PUMA complex; A. Prestel for expert NMR assistance; S. S. Sjørup and C. O'Shea for technical support and protein purification; A. S. Hebbelstrup, C. B. Parsbæk and K. Teilum for the MCL1 construct; J. D. Calvete for graphical support; A. Chowdhury for comments on the manuscript and D. Nettels for providing data analysis tools. This work was supported by the Novo Nordisk Foundation challenge grant REPIN, rethinking protein interactions (NNF18OC0033926 to K.S., B.S. and B.B.K.), by the Danish Research Councils (9040-00164B to B.B.K.), and by the Swiss National Science Foundation (310030_197776 to B.S.). Further support was given by the European Union's Horizon 2020 research and innovation programme under the Marie Sklodowska-Curie grant agreement 101023654 (awarded to E.A.N.). NMR spectra were recorded at cOpenNMR, an infrastructure facility funded by the Novo Nordisk Foundation (NNF18OC0032996).

Author contributions This study was conceptualized by J.G.O., E.A.N., A.D.D., L.S., K.B., K.S. and B.B.K. J.G.O., L.S., K.B. and C.R.O.B. designed the D-peptides. E.A.N. carried out experiments on ProTα and MCL1 presented in this manuscript, with initial experiments on ProTα conducted by C.B.F. and K.B. smFRET was performed by A.S. in collaboration with B.S. A.D.D. carried out the experiments with RST presented in the manuscript, except for the ZZ-exchange and R_2 measurements on ANAC013, which were done by S.E., and the ionic strength dependence of K_d values, which was done by A.D.D. and F.F.T. F.F.T. extracted the correlation in Fig. 4g. Initial experiments were conducted by E.D., I.B. and L.S. E.A.N., A.D.D., K.S., J.G.O. and B.B.K. wrote the manuscript with contributions from all authors. All authors have read and agreed to the submitted and published version of the manuscript.

Competing interests The authors declare no competing interests.

Additional information

Supplementary information The online version contains supplementary material available at https://doi.org/10.1038/s41586-024-08271-6.

Correspondence and requests for materials should be addressed to Johan G. Olsen or Birthe B. Kragelund.

Peer review information *Nature* thanks the anonymous reviewer(s) for their contribution to the peer review of this work. Peer review reports are available.

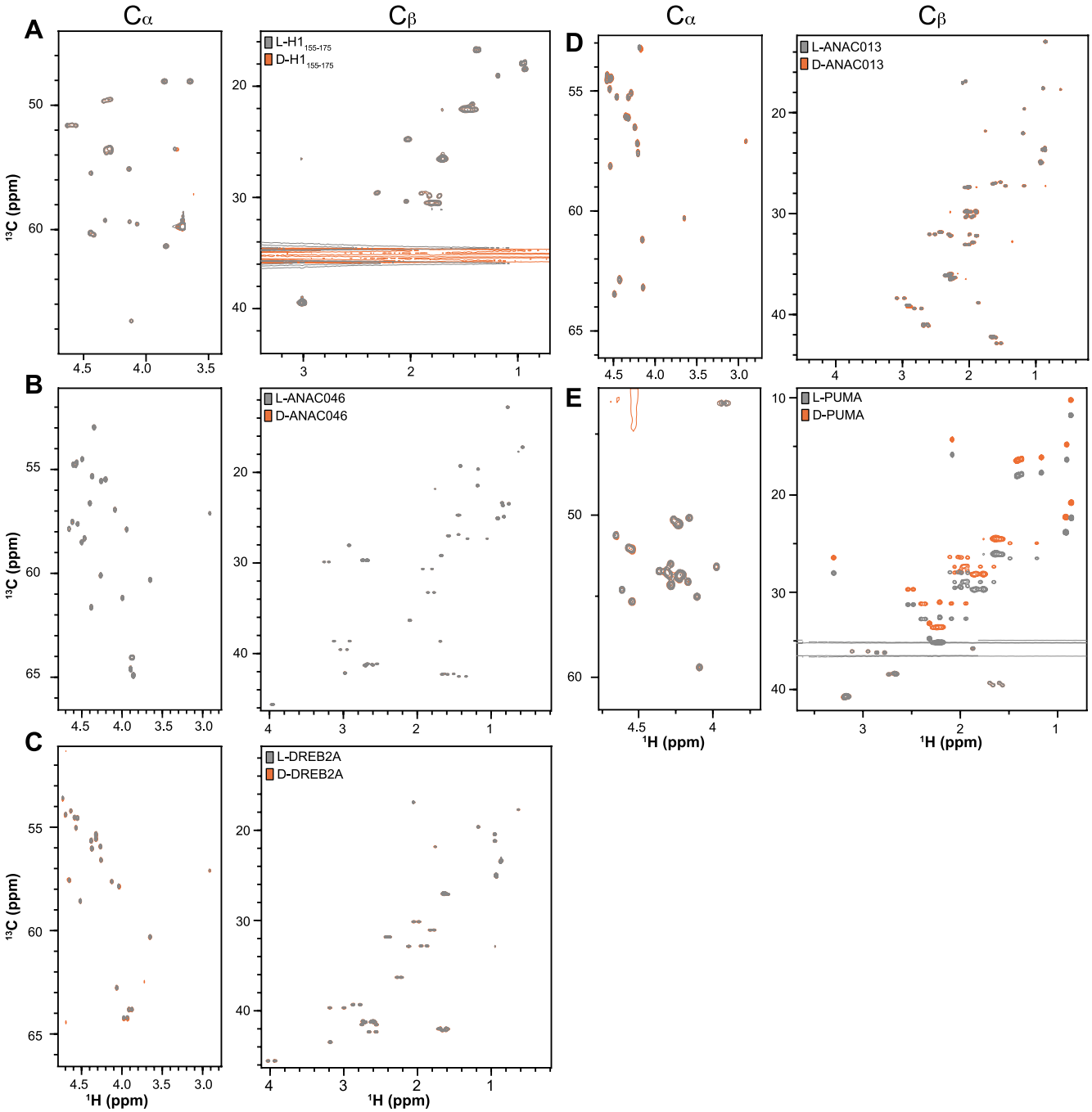

Extended Data Fig. 1 | ^{13}C-HSQC NMR spectra showing C^{α} and C^{β} chemical shifts of L- and D-peptides. A L-H1$_{155\text{-}175}$ and D-H1$_{155\text{-}175}$; B L-ANAC046 and D-ANAC046; C L-DREB2A and D-DREB2A; D L-ANAC013 and D-ANAC013; E L-PUMA and D-PUMA. All L-peptides displayed in grey and D-peptides in orange. For A and E, a line at 35 ppm in the ^{13}C-dimension originates from the presence of Tris in the buffer.

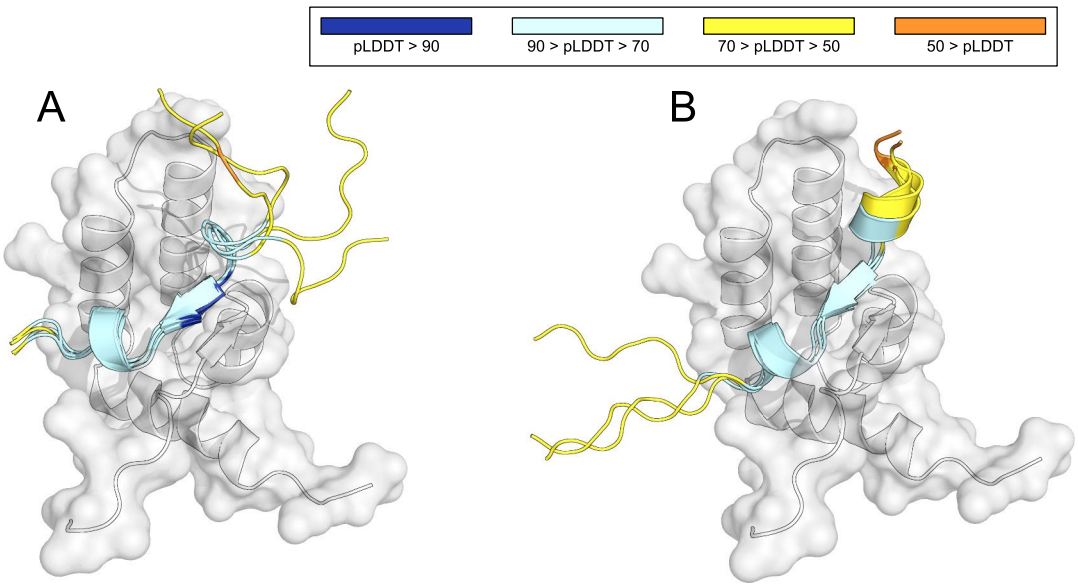

Extended Data Fig. 2 | AlphaFold3 models of ANAC046 and ANAC013 peptides in complex with RST. Peptide models agreeing with experimental data colored according to the pLDDT of ANAC046 (A) and ANAC013 (B). RST is shown in grey in a representative conformation to ease the comparison of the peptide models. The color scheme is shown at the top and matches the scale used by Alphafold3. PyMol version 2.6.0a0 was used to visualise the structures.

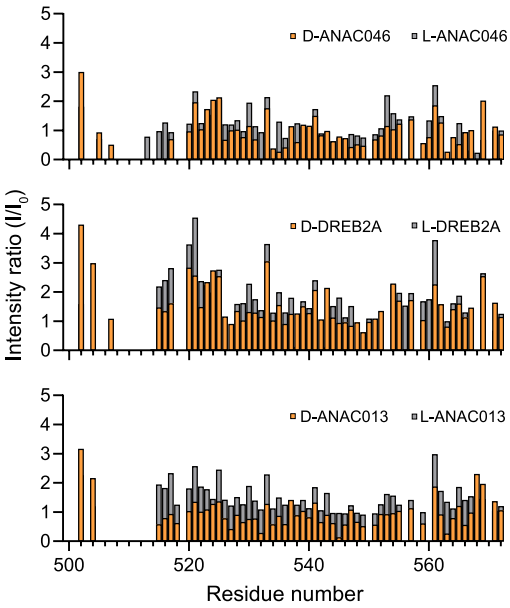

Extended Data Fig. 3 | Comparison of NMR peak intensities from binding L- and D-enantiomers to RST. Intensity ratios reported for the interactions of RST with D- (orange) and L-version (grey) of ANAC046$_{319\text{-}338}$ (top), DREB2A$_{255\text{-}272}$ (middle), and ANAC013$_{254\text{-}274}$ (bottom). The saturation was in all cases 99% or above.

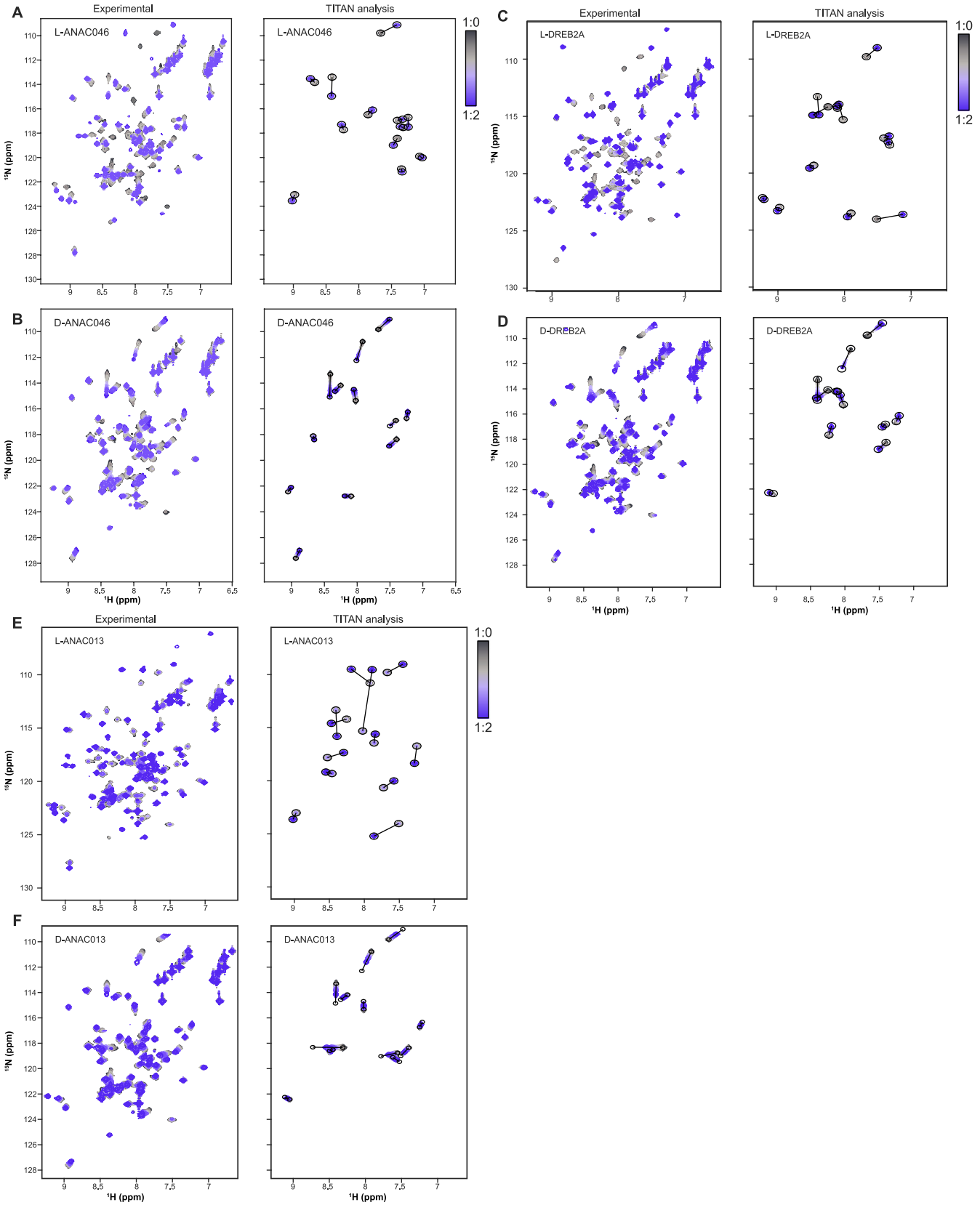

Extended Data Fig. 4 | NMR lineshape analysis of titration of RST with RST-interacting peptides using TITAN[31]. **A** L-ANAC046; **B** D-ANAC046; **C** L-DREB2A; **D** D-DREB2A; **E** L-ANAC013; **F** D-ANAC013. A concentration range of 0, 20, 40, 60, 80, 100, and 200 µM peptide (final concentration in sample) was titrated into ^{15}N-RST with a concentration of 100 µM.

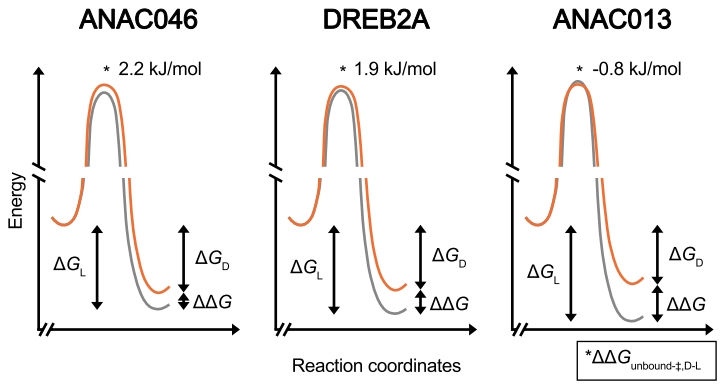

Extended Data Fig. 5 | Free energy diagrams of transcription factor-peptide interactions with RST. Differences in binding free energies, $\Delta\Delta G$ from ITC and differences in activation free energies between D- and L-peptides, $\Delta\Delta G_{\text{unbound-‡,D-L}}$, from NMR lineshape analysis (Extended Data Fig. 4, Extended Data Table 3). (orange: D; gray: L).

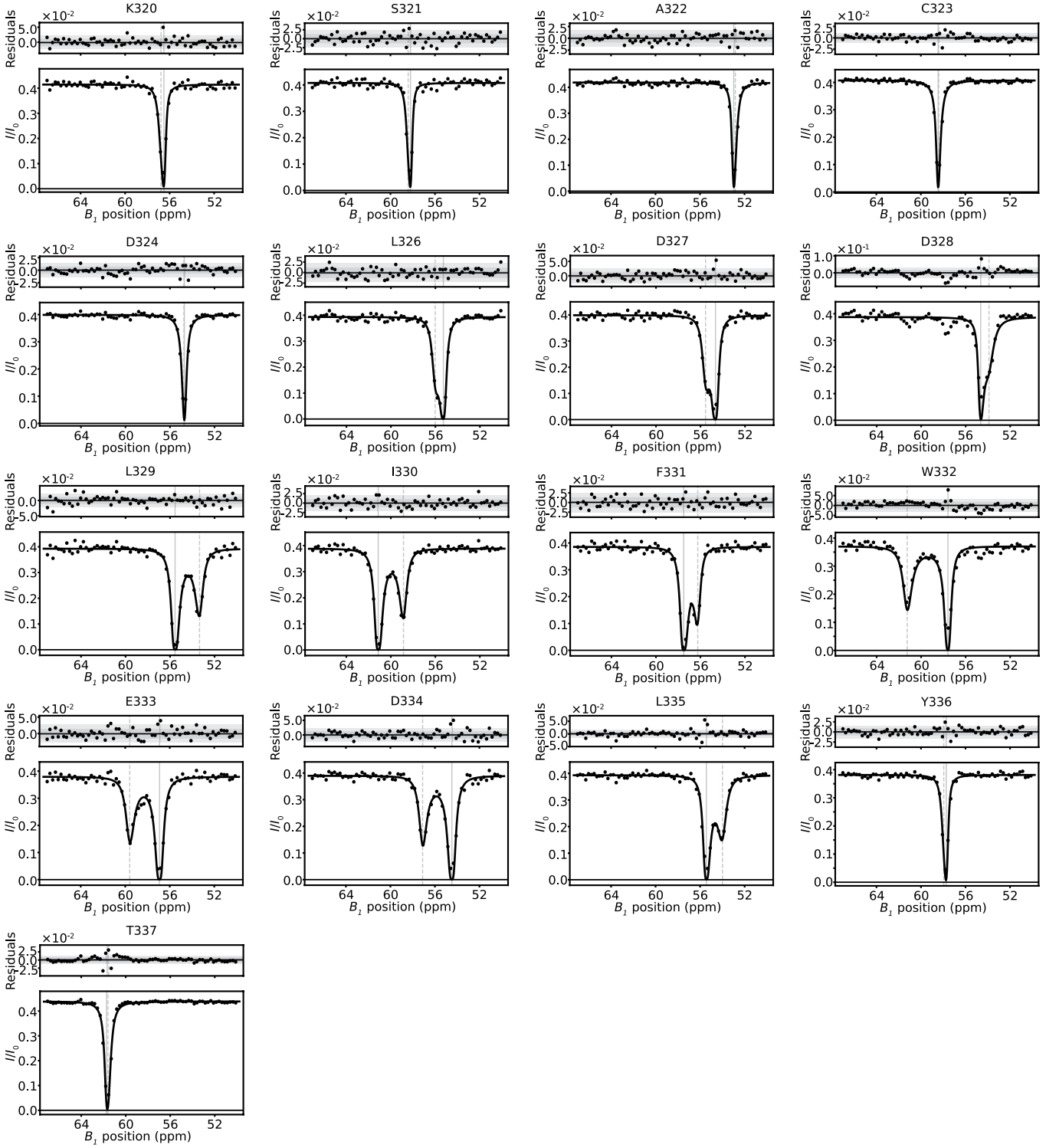

Extended Data Fig. 6 | C^{α}-CEST profiles of ^{13}C,^{15}N-labeled L-ANAC046$_{319\text{-}338}$ peptide with 5% RST. A concentration of 1 mM ^{13}C,^{15}N-L-ANAC046$_{319\text{-}338}$ with 50 µM RST was used in the CEST experiment to ensure 5% saturation based on the Kd from ITC. The used pulse sequences modulate HSQCs as a function of i−1 carbon saturation. Hence the HSQC peak of residue e.g. S321 is modulated as a function of K320 carbon saturation. The profiles shown correspond to the C^{α} of the residue given at each plot. The pulse sequence used cannot probe the C^{α} of G325 in the peptide. The dots show the experimental data while the line shows the fit. The vertical grey dotted, and solid lines correspond to the chemical shift given from the fit of the peptide's unbound and bound states, respectively. Residuals are shown above each plot. The additional smaller dips in the CEST profile of D328 could not be recaptured in the ^{15}N-CEST or $^{13}C'$-CEST profiles, suggesting they originate form noise.

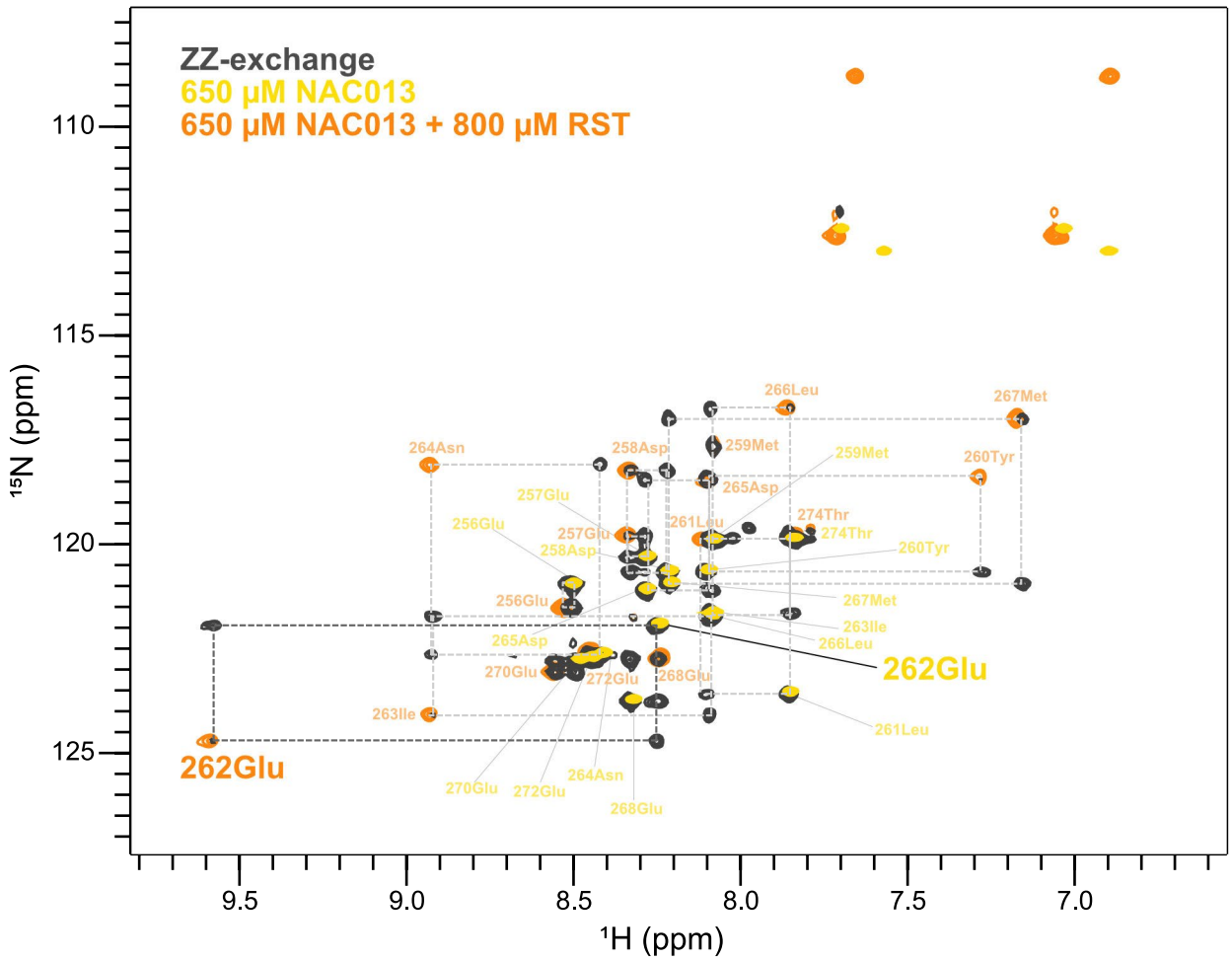

Extended Data Fig. 7 | ZZ-exchange NMR spectroscopy of L-ANAC013 in complex with RCD1-RST at 25 °C. The ZZ-exchange spectrum of L-ANAC013 (100 µM L-ANAC013 + 50 µM RST, grey) is overlayed with L-ANAC013 in its free (650 µM L-ANAC013, yellow) and bound form (650 µM L-ANAC013 + 800 µM RST, orange). The dashed lines connect the peaks from the free state to those of the bound state via ZZ-exchange cross-peaks. Example highlighted for Glu262.

Extended Data Table 1 | CIDER[65] analysis of disordered peptides

Peptide	Sequence	No. residues	Fraction charged residues (FCR)	Net charge per residue (NCPR)	Kappa (κ)	Hydropathy
H1155-175	KKAKKPKTVKAKPVKASKPKK	21	0.52	0.52	0.10	2.81
ANAC046319-338	SKSACDGLDDLIFWEDLYTS	20	0.30	-0.20	0.35	4.30
DREB2A255-272	SSDMFDVDELLRDLNGDD	18	0.44	-0.33	0.23	3.71
ANAC013254-274	NLEEDMYLEINDLMEPEPEPT	21	0.38	-0.38	0.08	3.45
PUMA130-156	EEEWAREIGAQLRRAADDLNAQYERRM	27	0.44	-0.07	0.13	3.13

Extended Data Table 2 | Thermodynamics and kinetics for L- and D-peptide interactions

Model systems		Thermodynamics					Kinetics		
		N	K_d (μM)	ΔH (kJ/mol)	-TΔS (kJ/mol)	ΔG (kJ/mol)	K_d (μM)	k_{off} (s^{-1})	k_{on} ($\mu M^{-1} \cdot s^{-1}$)
ProTα	L-H1$_{155-175}$	1*	8 ± 3	-87 ± 22	63 ± 24	-29 ± 1	-	-	-
	D-H1$_{155-175}$	1*	8 ± 0.6	-90 ± 6	70 ± 6	-28 ± 0.3	-	-	-
RCD1-RST$_{409-572}$	L-ANAC046$_{319-338}$	0.93 ± 0.02	0.67 ± 0.05	-25 ± 1	-10 ± 1	-35.3 ± 0.2	0.27 ± 0.02	101 ± 3	370 ± 30
	D-ANAC046$_{319-338}$	0.85 ± 0.02	10 ± 2	-23 ± 1	-5 ± 2	-28.5 ± 0.4	10.8 ± 0.5	1664 ± 84	154 ± 10
	L-DREB2A$_{255-272}$	0.85 ± 0.07	0.25 ± 0.03	-61 ± 2	23 ± 2	-37.7 ± 0.3	0.13 ± 0.01	47 ± 1	370 ± 30
	D-DREB2A$_{255-272}$	0.85 ± 0.05	18 ± 5	-23 ± 2	-5 ± 2	-27.2 ± 0.6	10.0 ± 0.5	1752 ± 121	175 ± 15
	L-ANAC013$_{254-274}$	0.95 ± 0.02	0.081 ± 0.001	-48 ± 1	8 ± 1	-40.48 ± 0.04	Fixed	7.0 ± 0.3	86 ± 4
	D-ANAC013$_{254-274}$	0.92 ± 0.07	41 ± 19	-8 ± 2	-17 ± 4	-25 ± 3	80 ± 6	9518 ± 598	118 ± 12
MCL1$_{152-308}$	L-PUMA$_{130-156}$	0.89 ± 0.02	0.0013 ± 0.0003	-93 ± 1	42 ± 1	-51.7 ± 0.6	-	-	-
	D-PUMA$_{130-156}$	0.41 ± 0.20	270 ± 39	-280 ± 55	259 ± 55	-20.8 ± 0.3	-	-	-

*Fixed at N = 1.

Fixed: K_d from ITC used as a fixed value in the 2D line-shape analysis.

Errors are standard errors of the mean from three technical replicates.

Extended Data Table 3 | Effects of stereochemistry on interactions

	$\Delta\Delta G_{D\text{-}L}$ (kJ/mol)	$\Delta\Delta H_{D\text{-}L}$ (kJ/mol)	$\Delta(-T\Delta S)_{D\text{-}L}$ (kJ/mol)	$\Delta\Delta G_{unbound\text{-}‡,D\text{-}L}$ (kJ/mol)
MCL1:PUMA	30.9 ± 0.7	-187 ± 55	218 ± 55	-
ProTα: H1$_{155\text{-}175}$	0.3 ± 1	-3 ± 23	7 ± 25	-
RCD1-RST:ANAC046	6.8 ± 0.4	2 ± 1	5 ± 2	2.2
RCD1-RST:DREB2A	10.5 ± 0.7	38 ± 3	-28 ± 3	-0.8
RCD1-RST:ANAC013	15 ± 3	40 ± 2	-25 ± 4	1.9

nature portfolio

Corresponding author(s): Birthe B. Kragelund, Johan G. Olsen

Last updated by author(s): Aug 26, 2024

Reporting Summary

Nature Portfolio wishes to improve the reproducibility of the work that we publish. This form provides structure for consistency and transparency in reporting. For further information on Nature Portfolio policies, see our Editorial Policies and the Editorial Policy Checklist.

Statistics

For all statistical analyses, confirm that the following items are present in the figure legend, table legend, main text, or Methods section.

n/a	Confirmed	
☐	☒	The exact sample size (*n*) for each experimental group/condition, given as a discrete number and unit of measurement
☐	☒	A statement on whether measurements were taken from distinct samples or whether the same sample was measured repeatedly
☒	☐	The statistical test(s) used AND whether they are one- or two-sided *Only common tests should be described solely by name; describe more complex techniques in the Methods section.*
☒	☐	A description of all covariates tested
☒	☐	A description of any assumptions or corrections, such as tests of normality and adjustment for multiple comparisons
☐	☒	A full description of the statistical parameters including central tendency (e.g. means) or other basic estimates (e.g. regression coefficient) AND variation (e.g. standard deviation) or associated estimates of uncertainty (e.g. confidence intervals)
☒	☐	For null hypothesis testing, the test statistic (e.g. *F*, *t*, *r*) with confidence intervals, effect sizes, degrees of freedom and *P* value noted *Give P values as exact values whenever suitable.*
☒	☐	For Bayesian analysis, information on the choice of priors and Markov chain Monte Carlo settings
☒	☐	For hierarchical and complex designs, identification of the appropriate level for tests and full reporting of outcomes
☒	☐	Estimates of effect sizes (e.g. Cohen's *d*, Pearson's *r*), indicating how they were calculated

Our web collection on statistics for biologists contains articles on many of the points above.

Software and code

Policy information about availability of computer code

Data collection	SymphoTime 64 version 2.4 (PicoQuant) was used for single molecule data collection. NMR data were recorded at cOpenNMR (supported by the Novo Nordisk Foundation) on Bruker instruments using Topspin versions 3.6.5, 4.0.7 or 4.2.0 (Bruker Biospin). CD data were recorded on Jasco J815 or J810 using SpectraManager from Jasco Inc. ITC data were collected on MicroCal PEAQ-ITC microcalorimeter (Malvern Panalytical, Malvern, United Kingdom) and on a MicroCal ITC200 microcalorimeter (MicroCal Instruments, Northampton, United Kingdom).
Data analysis	Fretica, a custom add-on package for Mathematica v.12.3 (Wolfram Research) was used for the analysis of single-molecule fluorescence data and is available at https://github.com/SchulerLab. For NMR data analyses, pMDD 60, NMRPipe, CcpNMR were used, otherwise GraphPad Prism 8.4.1 and SpectraManager (Jasoc Inc), Origen 7, TITAN, Jasco software for CD, ChemEX for CEST.ITC data were analysed using Origin7 or Malvern Panalytical analysis software

For manuscripts utilizing custom algorithms or software that are central to the research but not yet described in published literature, software must be made available to editors and reviewers. We strongly encourage code deposition in a community repository (e.g. GitHub). See the Nature Portfolio guidelines for submitting code & software for further information.

Data

Policy information about availability of data

All manuscripts must include a data availability statement. This statement should provide the following information, where applicable:

- Accession codes, unique identifiers, or web links for publicly available datasets
- A description of any restrictions on data availability
- For clinical datasets or third party data, please ensure that the statement adheres to our policy

Chemical shifts of MCL1 in the PUMA bound state have been submitted to BioMagResBank under the accession number 52264

Research involving human participants, their data, or biological material

Policy information about studies with human participants or human data. See also policy information about sex, gender (identity/presentation), and sexual orientation and race, ethnicity and racism.

Reporting on sex and gender	not relevant
Reporting on race, ethnicity, or other socially relevant groupings	not relevant
Population characteristics	not relevant
Recruitment	not relevant
Ethics oversight	not relevant

Note that full information on the approval of the study protocol must also be provided in the manuscript.

Field-specific reporting

Please select the one below that is the best fit for your research. If you are not sure, read the appropriate sections before making your selection.

☒ Life sciences ☐ Behavioural & social sciences ☐ Ecological, evolutionary & environmental sciences

For a reference copy of the document with all sections, see nature.com/documents/nr-reporting-summary-flat.pdf

Life sciences study design

All studies must disclose on these points even when the disclosure is negative.

Sample size	The sample size for all free diffusion FRET experiments was always > 4000 freely diffusing molecules. The sample sizes were found to satisfactorily describe the conformational distributions and dynamics in the ensembles. For NMR, ITC and CD, the sample sizes were based on previous comparable experiments.
Data exclusions	Bursts arising from freely diffusing molecules with only a single fluorophore and with < 50 photons were excluded from analysis. More details on Data exclusion and selection can be found in the Methods section. For NMR analyses and protein interactions measurements, data were not excluded. For ITC, the first injection point was excluded do to the possibility of air in the injection volume.
Replication	The overall reproducibility of the main experiments was confirmed by making multiple independent measurements. For NMR analyses, data were recorded once except for the relaxation data, where data were recorded in triplicate on the same sample to extract error bars. ITC was recorded in triplicates or duplicates.
Randomization	No randomization was done
Blinding	Experiments were not blinded

Reporting for specific materials, systems and methods

We require information from authors about some types of materials, experimental systems and methods used in many studies. Here, indicate whether each material, system or method listed is relevant to your study. If you are not sure if a list item applies to your research, read the appropriate section before selecting a response.

Materials & experimental systems

n/a	Involved in the study
☒	☐ Antibodies
☒	☐ Eukaryotic cell lines
☒	☐ Palaeontology and archaeology
☒	☐ Animals and other organisms
☒	☐ Clinical data
☒	☐ Dual use research of concern
☒	☐ Plants

Methods

n/a	Involved in the study
☒	☐ ChIP-seq
☒	☐ Flow cytometry
☒	☐ MRI-based neuroimaging

Plants

Seed stocks: not relevant

Novel plant genotypes: not relevant

Authentication: not relevant